



A combined experimental–numerical investigation of ductile fracture in bending of a class of ferritic–martensitic steel

C. Soyarslan*, M. Malekipour Gharbi, A.E. Tekkaya

Institut für Umformtechnik und Leichtbau, Technische Universität Dortmund, 44227 Dortmund, Germany

ARTICLE INFO

Article history:

Received 24 October 2011

Received in revised form 2 March 2012

Available online 27 March 2012

Keywords:

Bending

Strain localization

Ductile fracture

Shear modified GTN model

Ferritic–martensitic steel

ABSTRACT

We present a combined experimental–numerical study on fracture initiation at the convex surface and its propagation during bending of a class of ferritic–martensitic steel. On the experimental side, so-called free bending experiments are conducted on DP1000 steel sheets until fracture, realizing optical and scanning electron microscopy analyses on the post mortem specimens for fracture characterization. A blended Mode I – Mode II fracture pattern, which is driven by cavitation at non-metallic inclusions as well as martensitic islands and resultant softening-based intense strain localization, is observed. Phenomena like crack zig-zagging and crack alternation at the bend apex along the bending axis are introduced and discussed. On the numerical side, based on this physical motivation, the process is simulated in 2D plane strain and 3D, using Gurson's dilatant plasticity model with a recent shear modification, strain-based void nucleation, and coalescence effects. The effect of certain material parameters (initial porosity, damage at coalescence and failure, shear modification term, etc.), plane strain constraint and mesh size on the localization and the fracture behavior are investigated in detail.

© 2012 Elsevier Ltd. All rights reserved.

1. Introduction

In metallic materials, the localization into deformation bands, as a precursor to fracture, is sourced from two strongly microstructure-dependent constitutive features, (1) path dependence of strain hardening and (2) softening mechanism (Asaro, 1985). The former is caused by destabilizing effects of the existence of a vertex or a region of sharp curvature at the loading point of the yield surface, which are implied by the stiffness reduction with respect to non-proportional load increments (Asaro, 1985; Becker, 1992). Such vertex formations are natural outcomes of the underlying physics of single crystals with the existence of discrete slip systems and accordingly resolved shear stresses. The latter may be due to the effect of temperature on mechanical properties (see e.g. Lemonds and Needleman, 1986), or progressive material deterioration due to cavitation, i.e. nucleation, growth, and coalescence of microvoids, see e.g. Yamamoto (1978), Needleman and Rice (1978), Saje et al. (1980) also Tvergaard (1982b).

Experiments reveal that fracture development in bending of modern alloys and polycrystals usually occurs with intense strain localization starting at the free convex surface, which is preceded by orange peels and gradually growing undulations parallel to the bend axis (Akeret, 1978; Sarkar et al., 2001; Dao and Lie, 2001; Lievers et al., 2003a). Numerical studies invariably use the

finite element method in investigations on bendability. In accordance with the mentioned constitutive strain localization sources, previous numerical studies on bending will be classified under the following categories:

- Path-dependent strain hardening,
- Softening,
- Combined path-dependent strain hardening and softening,

with a brief summary of approaches is given below. For convenience reasons, we also list these studies in historical order in Table 1.

Becker (1992) investigates pure bending of a polycrystalline sheet using a slip-based Taylor-like polycrystal model. The effect of inherent inhomogeneity with incompatibility of neighboring grains by different sets of crystal orientations at each grain and its effect on the shear band initiation at the free surface and its propagation toward the neutral axis is studied. Using a crystal plasticity-based model, Dao and Lie (2001) investigate the localization and fracture initiation (generally in a transgranular fashion) during bending of aluminum alloy sheets. Like in Triantafyllidis et al. (1982), Becker (1992) and Kuroda and Tvergaard (2007) the localizations are observed at both convex and concave surfaces. It is shown that without constituent particles intense shear bands initiate from wave bottoms whereas a localization in the form of shear bending can start beneath the free surface with the inhomogeneity effect of second-phase particles. The most important

* Corresponding author.

E-mail address: celal.soyarslan@iul.tu-dortmund.de (C. Soyarslan).

Table 1

Studies on localization and fracture in bending of metallic sheets.

ID	Reference	Model	Material	Crack propagation
1	Tvergaard (1981)	GTN	Al 6000	✓
2	Triantafyllidis et al. (1982)	Corner Theory	Hypothetical	–
3	Tvergaard (1987)	GTN + Kin. Hard.	Hypothetical	–
4	Becker (1992)	Crystal Plasticity	Polycrystal Al	✓
5	Kuroda and Tvergaard (2001)	Non-associative Flow	Hypothetical	–
6	Dao and Lie (2001)	Crystal Plasticity	Hypothetical	–
7	Hambli et al. (2003)	CDM	Hypothetical	–
8	Lievers et al. (2003a)	GTN + Kin. Hard.	AA6111	–
9	Lievers et al. (2003b)	GTN + Kin. Hard.	Hypothetical	✓
10	Hambli et al. (2004)	CDM	0.6% C-Steel	✓
11	Wisselink and Huetink (2007)	Nonlocal CDM	Hypothetical	✓
12	Wisselink and Huetink (2008)	Nonlocal CDM	Al 6016	✓
13	Xue and Wierzbicki (2008)	CDM	Al 2014-T351	✓
14	Le Maout et al. (2009)	GTN	Al 6000	✓
15	Kim et al. (2010)	Thermal Softening	DP 780	–
16	Bettaieb et al. (2010a,b)	GTN + Kin. Hard.	DP 600	–

factors affecting bending of aluminum sheets are found to be strain hardening, texture, second phase particle position, and distribution, where high strain hardening is found to reduce the susceptibility to localization. Finally, using a generalized Taylor type polycrystal model, Kuroda and Tvergaard (2007) model bending localizations. Triantafyllidis et al. (1982) study localization and shear band development in pure bending of elastoplastic solids with sharp and blunt vertices, respectively, using the J_2 corner theory presented in Christoffersen et al. (1979). Wavelength imperfections are applied which focus on the deformation into shear bands starting from the free surface. It is notable that initial localizations are captured in the concave surface rather than the convex one in this study. Finally, Kuroda and Tvergaard (2004) present plane strain bending localizations with a material model involving non-associative plastic flow as given in Kuroda and Tvergaard (2001).

Coming to softening-based models, Kim et al. (2010) use thermo-mechanical coupling to model draw-bending where adiabatic thermal softening acts as the localization agent, with the condition of a maximum tensile force, i.e. $dF = 0$, being set as the condition of localization. This study does not investigate crack modes and crack patterns.

Damage softening is taken into account through internal variables which phenomenologically reflect the stiffness and strength loss of the matter, as in the case of Continuum Damage Mechanics (CDM) models, or via dilatancy of macroscopic plasticity and cavitation, as in the case of Gurson's plasticity.

Starting with the former, using a (gradient type) nonlocally enhanced CDM model, Wisselink and Huetink (2007) and Wisselink and Huetink (2008) present mesh objective softening-induced strain localization (where bifurcation into two crossing shear bands occurs) and crack trajectories in bending. The effect of pre-strain is investigated where the prestrained specimens are shown to fail earlier, Wisselink and Huetink (2008). Xue and Wierzbicki (2008) investigate the bendability of 2024-T351 Al alloys using a phenomenological model where the plane strain (shear) effects are involved through the utilization of load angle dependence. For sheets having different width-thickness-ratios it is experimentally and numerically shown that cracks start with shear localization at the central zone with the plane strain constraint. Hambli et al. (2003) use a Lemaitre type CDM model for the L-bending process with plane strain assumption. Unlike in previously mentioned studies damage development is seen at both convex and concave sides of the bend at the same orders of magnitude. These questionable results stem from the utilized tension-compression invariant damage growth formulation which does not involve quasi-unilateral effects. This study does not involve localization due to a relatively coarse adapted mesh which acts as a length scale. Identical

comments apply to Hambli et al. (2004) in which another CDM model with the damage evolution relying on equivalent plastic strain and its rate is used to evaluate bending defects. Since this study focuses on a variant of Gurson's plasticity, theoretical details of the CDM models are beyond our scope. Interested readers can refer to the texts of Lemaitre (1996) and Lemaitre and Desmorat (2005) for fundamentals or the manuscripts, and Brunig (2003), Brunig and Ricci (2005), Bonora et al. (2005), Menzel et al. (2005), Bonora et al. (2006), Pironi et al. (2006), Soyarslan et al. (2008), Soyarslan and Tekkaya (2010) and Badreddine et al. (2010) and more recently Malekipour Gharbi et al. (2011) for certain developed advanced finite strain frameworks and various applications.

Coming to the latter, Tvergaard (1982b) investigates shear band localization in pure bending with cavitation under the effect of surface waviness and material inhomogeneity through concentrated local sub-surface void nucleating particles. In the progressively cavitating model localization occurs faster at the apex of the bend as opposed to Triantafyllidis et al. (1982) since the void growth is hindered on the compressive side of the neutral axis. Without specific reference to localization modes or fracture patterns, Le Maout et al. (2009) investigate a hemming process for 6000 series aluminum alloys using Gurson's damage model with Hill 48 type plastic anisotropy.

For the combined effects of path-dependent strain hardening and cavitation Tvergaard (1987) constitutes an example where shear cracks developed from void sheets inside the localization bands are modeled with Gurson's porous plasticity which gives account for progressive cavitation with combined effects of kinematic and isotropic hardening on the yield surface curvature following Mear and Hutchinson (1985). Kinematic hardening, by introducing an increased curvature compared to a merely isotropic hardening one, adds imperfection sensitivity to the constitutive model due to slight additional load path changes. The degree of non-uniformity of the strain field by an enforcement of the surface waviness causes a shear band formation at the wave bottoms. As noted by Tvergaard (1987), the results admit a length-scale where strong mesh-dependence is due. For smaller element sizes narrower yet earlier localization bands are carried out. Lievers et al. (2003a) study bendability of AA6111 sheets for different Fe concentrations using Gurson's model with isotropic and kinematic hardening effects where the surface roughness effect is also investigated. Together with an alternative formulation of kinematic hardening Lievers et al. (2003b) investigate the localization in bending using Gurson's damage model on the same problem example as Tvergaard (1987). A systematic sensitivity analysis is followed through many material parameters related to yield

surface curvature, material gradient, and failure mode. Again, it is also shown that geometric imperfections amplify the strain gradients and act as strain concentrators. Finally, [Bettaieb et al. \(2010\)](#), using Gurson's damage model with kinematic hardening effects and Thomason type void coalescence developed in [Bettaieb et al. \(2010a\)](#), study bending fractures by means of finite element analyses, also studying the effect of geometric imperfections.

This study aims at presenting a combined experimental and numerical analysis on bending of a class of ferritic–martensitic steel. Ferritic–martensitic steels are commonly utilized in automotive industry due to their lightweight characteristics and good stretching performance. However, their formability is limited by fracture originating from voidage with growth and the coalescence of micro-voids which nucleate with decohesion at matrix non-metallic inclusions ($\sim 5\text{--}30\text{ }\mu\text{m}$ in diameter) or ferrite–martensite interfaces as well as inclusions or dispersed martensite particle ($\sim 0.5\text{ }\mu\text{m}$ in diameter) cracking. This cavitation history strongly depends on the stress state during plastic flow. The triaxial tensile (compressive) stress states give account for exponential void growth (shrinkage), whereas void sheeting, void nucleation, void distortion and void interaction with material rotation promotes a degradation of stiffness and strength under the shear stress states.

On the experimental part, we present a fractography analysis of a set of DP1000 steel sheets which are bent until fracture with the free bending process. At certain loading levels Light Optical Microscopy (LOM) investigations are realized on the convex surface of the bend in order to capture surface undulations which, as aforementioned, motivate strain localization throughout the rest of the loading. Similar mechanisms until incipient fracture at the wave bottom, observed by [Akeret \(1978\)](#) and [Sarkar et al. \(2001\)](#), are captured for this class of advanced high strength steels as well. Once the apex of the bent and cracked specimens is investigated it is seen that the crack follows alternate patterns which are discontinuous on the bending axis. Such a pattern which cannot be captured in a plane strain analysis is linked to local material inhomogeneities throughout the bending axis. Coming to the fracture patterns at planes orthogonal to the bend axis, the observations invariably show crack initiation with an angle to the maximum tensile loading direction which holds the sign of a developed shear localization at the incipient fracture. It is observed that the cracks tend to evolve following a zig-zag pattern in the form of periodic ridges and valleys, which are characteristic for fracture surfaces separated by homogeneous micro-void fracture, [Beachem and Yoder \(1973\)](#). An elucidation of this phenomenon based on different sources is given. In order to clarify the mode of the fracture, SEM analyses are conducted focusing on post-mortem fractured surfaces. Considerable evidence for cavitation, as a sign of void sheeting and resulting localization, is observed where the parabolic dimples, taking into account the macroscopic loading conditions, give a sign of a blended condition of the transgranular fracture of Mode I and Mode II (using the elastic fracture mechanics notion), with a domination of Mode II.

On the numerical part, bending is simulated using 2D plane strain and 3D finite element models which aim at capturing not only initial localization into shear bands at the convex free surface, but also the crack propagation and the crack path. For this purpose, a finite strain hypoelastic–plasticity framework with Gurson's porous model including a recent shear modification, [Nahshon and Hutchinson \(2008\)](#), is developed and algorithmic steps for local integrations, which use a class of cutting plane algorithms, [Ortiz and Simo \(1986\)](#), are derived. Since DP1000 shows a relatively weak anisotropy due to rolling, this study is limited to the plastic isotropy. To this end, the derivations are implemented as a VUMAT subroutine for ABAQUS/ EXPLICIT. Our motivation regarding the selection of a porous plasticity model, where softening is the prime localization source, stems from the aforementioned experimental

evidence of cavitation on fracture surfaces. With this model, in accordance with [Tvergaard \(1982b\)](#) and [Tvergaard \(1987\)](#), we capture the localization on the convex surface of the bend under tension since the concave surface does not give account for void growth due to compressive hydrostatic stress. It should be noted that without sufficient softening a localization pattern cannot be captured according to [Xue and Wierzbicki \(2008\)](#). Under generalized plane strain conditions (pure shear plus hydrostatic stress) materials are more susceptible to fracturing compared to generalized compressive or tensile stress states on the Π plane, i.e. for equal pressure values, [Xue and Wierzbicki \(2008\)](#). This experimental fact is resolved by [Xue and Wierzbicki \(2008\)](#) by making use of Lode parameter dependence, which distinguishes generalized plane strain states from axisymmetric stress states, of void growth in Gurson's damage model. [Nahshon and Hutchinson \(2008\)](#) uses a third invariant of the deviatoric Cauchy (true) stress tensor for this purpose. We present a number of sensitivity analyses based on mesh size and damage-related material parameters. It is observed that selected mesh size acts as a length scale and manipulates localization time and width, in accordance with the findings of [Tvergaard \(1987\)](#). Moreover, it is shown that a small damage threshold for fracture results in a fracture pattern orthogonal to the principal tensile stress direction which occurs prior to shear band development resembling a brittle cleavage type separation, see also [Lievers et al. \(2003a\)](#). Regarding the crack pattern, zig-zagging is qualitatively captured which, on numerical grounds, is attributed to the combined effect of macroscopic loading conditions and the shear band crossing, where the physical motivations are attributed to different phenomena.

The remaining paper has the following outline. Section 2 summarizes shear enhanced Gurson's porous plasticity where the numerical implementation takes place in the appendices. Section 3 and Section 4 respectively present a detailed analysis regarding DP1000's microstructure, experimental results with optical and scanning electron microscopy, and numerical modeling results with 2D plane strain and 3D finite elements. Finally, conclusions are drawn and future perspectives are presented in Section 5.

In the paper, the following notations will be used. Consistently assuming \mathbf{a} , \mathbf{b} , and \mathbf{c} as three second order tensors, together with the Einstein's summation convention on repeated indices, $\mathbf{c} = \mathbf{a} \bullet \mathbf{b}$ represents the single contraction product with $[c]_{ik} = [a]_{ij}[b]_{jk}$. This product also preserves its structure in between vectors and matrices. $d = \mathbf{a} : \mathbf{b}$ represents the double contraction product with $d = [a]_{ij}[b]_{ij}$, where d is a scalar. $\mathbb{E} = \mathbf{a} \otimes \mathbf{b}$, $\mathbb{F} = \mathbf{a} \oplus \mathbf{b}$, and $\mathbb{G} = \mathbf{a} \ominus \mathbf{b}$ represent the tensor products with $[\mathbb{E}]_{ijkl} = [a]_{ij}[b]_{kl}$, $[\mathbb{F}]_{ijkl} = [a]_{ik}[b]_{jl}$, and $[\mathbb{G}]_{ijkl} = [a]_{il}[b]_{jk}$, where \mathbb{E} , \mathbb{F} , and \mathbb{G} represent fourth order tensors. $[\star]^t$ and $[\star]^{-1}$ denote the transpose and the inverse of $[\star]$ respectively. $\partial_{\mathbf{A}}[\star]$ and $\partial_{\mathbf{AA}}^2[\star]$ respectively denote $\partial[\star]/\partial\mathbf{A}$ and $\partial^2[\star]/\partial\mathbf{A} \otimes \partial\mathbf{A}$. $\text{dev}[\star]$ and $\text{tr}[\star]$ stand for a deviatoric part of and trace of $[\star]$, respectively, where $\text{dev}[\star] = \star - 1/3\text{tr}[\star]\mathbf{1}$, with $\text{tr}[\star] = [\star]_{ii}$ and $\mathbf{1}$ denoting the identity tensor. $[\star]^{sym}$ and $[\star]^{skw}$ denote symmetric and skew-symmetric portions of $[\star]$. $\partial_t[\star]$ gives the material time derivative of $[\star]$, and $\langle \star \rangle = 1/2(\star + |\star|)$. Finally, $[\hat{\star}]$ gives any $[\star]$ represented at the rotationally neutralized, i.e. corotational, configuration.

2. Shear enhanced GTN damage model

For the hydrostatic stress-independent classical von Mises plasticity one has $\Phi^p = \Phi^p[\text{dev}[\mathbf{T}], e^p]$, with e^p denoting the equivalent plastic strain. Our formulation is based on the Gurson's generic scalar valued isotropic yield function, [Gurson \(1977\)](#), taking as a basis the response of a representative volume element containing a matrix of an incompressible ideal plasticity and a spherical void whose homogenization results in a macroscopically compressible

plasticity model. Assuming σ_y and e^p denote the virgin yield stress and the equivalent plastic strain of the undamaged material matrix with

$$\sigma_y = \sigma_0 + q[e^p], \quad (1)$$

where $q[e^p]$ represents the matrix material hardening function. Allowing f to represent the void volume fraction, one has $\Phi^p = \Phi^p[\text{dev}[\mathbf{T}], \text{tr}[\mathbf{T}], f, e^p]$ with

$$\Phi^p = \left(\frac{\sigma_{eq}}{\sigma_y} \right)^2 + 2q_1 f^* \cosh \left[\frac{3}{2} \frac{q_2 \sigma_m}{\sigma_y} \right] - (1 + q_3 f^{*2}) = 0, \quad (2)$$

where $\sigma_{eq} = \sigma_{eq}[\text{dev}[\mathbf{T}]]$ is the (macroscopic) equivalent von Mises stress, a function of Cauchy stress tensor, \mathbf{T} . q_1, q_2 , and q_3 are the material parameters, see e.g. Tvergaard (1981) and Tvergaard (1982a). For $q_1 = q_2 = q_3 = 1$ Gurson's original model, Gurson (1977), is recovered. For $q_1 = q_3 = 0$ the porous structure is lost, e.g. the pressure dependence is precluded and conventional iso-choric-isotropic plasticity is recovered. f^* denotes the modified void volume fraction, giving account for the accelerating effects of the void coalescence, Tvergaard and Needleman (1984),

$$f^* = \begin{cases} f & f \leq f_c, \\ f_c + \frac{f_f - f_c}{f_f - f_c} (f - f_c) & f > f_c. \end{cases} \quad (3)$$

where f_c is the critical void volume fraction at incipient coalescence. f_f is the fraction at failure. The material parameter f_u^* is defined by $f_u^* = 1/q_1$. The coalescence phase can be linked to an effective plastic strain rate, as seen in Oudin et al. (1995). A Thomason type void coalescence is used in Bettaieb et al. (2010a).

The plastic strain rate follows a conventional normality postulate,

$$\partial_t \mathbf{E}^p = \dot{\gamma} \partial_{\mathbf{T}} \Phi^p, \quad (4)$$

where $\dot{\gamma}$ is the plastic multiplier which is computed by the consistency condition. The hydrostatic stress-dependent yield function dictates a non-vanishing trace of $\partial_t \mathbf{E}^p$, i.e. $\text{tr}[\partial_t \mathbf{E}^p] \neq 0$. The rate $\partial_t e^p$ is defined by the following generalized plastic work equivalence relation via $(1 - f)\sigma_y \partial_t e^p = \mathbf{T} : \partial_t \mathbf{E}^p$,

$$\partial_t e^p = \frac{\mathbf{T} : \partial_t \mathbf{E}^p}{(1 - f)\sigma_y} \quad (5)$$

The void volume fraction is assumed to evolve in two phases, namely nucleation and growth, where the resulting form reads

$$\partial_t f = \partial_t f^n + \partial_t f^g, \quad (6)$$

with the superscripts; n and g stand for nucleation and growth, respectively. The void volume fraction due to nucleation depends on the equivalent plastic strain by

$$\partial_t f^n = A_N \partial_t e^p, \quad A_N = A_N(e^p) = \frac{f_N}{S_N \sqrt{2\pi}} \exp \left[-\frac{(e^p - e_N^p)^2}{2(S_N)^2} \right] \quad (7)$$

where f_N and S_N are the nucleated void volume fraction and Gaussian standard deviation, respectively. e_N^p denotes the mean equivalent plastic strain at the incipient nucleation. f_N, S_N and e_N^p are typical material parameters. In the classical Gurson's damage model the time rate of change of void volume fraction due to void growth is linked to the plastic dilatation under hydrostatic stress using $\partial_t f^g = \partial_t f_{hyd}^g$ where

$$\partial_t f_{hyd}^g = (1 - f) \text{tr}[\partial_t \mathbf{E}^p]. \quad (8)$$

Unless the mean stress is positive, this expression does not predict any damage development, subsequent localization with softening and fracture which is not in correlation with the experimental findings reported in e.g. Bao and Wierzbicki (2004) and Barsoum and Faleskog (2007). Nahshon and Hutchinson (2008) modified $\partial_t f^g$ to

give account for fracture for low and negative stress triaxialities to give $\partial_t f^g = \partial_t f_{hyd}^g + \partial_t f_{shr}^g$. $\partial_t f_{shr}^g$ relates to the effect of shear in damage growth and is defined as the following form scaled by the material parameter k_w

$$\partial_t f_{shr}^g = k_w f \frac{w(\text{dev}[\mathbf{T}])}{\sigma_{eq}} \text{dev}[\mathbf{T}]. \quad (9)$$

Accordingly, besides the exponential dependence of the void growth on triaxiality, softening and localization with mechanisms such as void distortion and void interaction with material rotation under shear is taken into account. A simple illustration of these two distinct stress state dependent microstructural mechanisms is given in Fig. 1. Note that although in the original Gurson's damage model f corresponds to a micro-mechanical variable, i.e. an average volumetric fraction of voids reflecting configurational changes, in the current extension it is a purely phenomenological one since f_{shr}^g does not denote an actual void growth but a qualitative indicator of the weakening under shear. To emphasize this fact, in the following pages, f and regarding components will be named as "damage" rather than void volume fraction.

The modification of Nahshon and Hutchinson (2008) proposes the dependence of void growth on the third invariant of the deviatoric stress tensor, which distinguishes the axisymmetric stress states from generalized plane strain states. The scalar valued tensor function $w(\text{dev}[\mathbf{T}])$ is defined as

$$w(\text{dev}[\mathbf{T}]) = 1 - \left(\frac{27J_3}{2\sigma_{eq}^3} \right)^2, \quad (10)$$

where J_3 is the third invariant of the deviatoric stress with $J_3 = (1/3)[\text{dev}[\mathbf{T}]]_{ij}[\text{dev}[\mathbf{T}]]_{jk}[\text{dev}[\mathbf{T}]]_{ki}$. For all axisymmetric stress states (which include the hydrostatic stress states) w vanishes where the classical Gurson's model is recovered. Depending on the relative success of classical Gurson's model for modeling localization and fracture under moderate to high stress triaxialities Nielsen and Tvergaard (2009) and Nielsen and Tvergaard (2010) introduced a triaxiality-dependent correction to w as follows,

$$w = w(\text{dev}[\mathbf{T}])\chi(\eta) \text{ with } \chi(\eta) = \begin{cases} 1 & \text{for } \eta < \eta_1 \\ (\eta - \eta_2)/(\eta_1 - \eta_2) & \text{for } \eta_1 < \eta < \eta_2, \\ 0 & \text{for } \eta > \eta_2 \end{cases} \quad (11)$$

where the correction applies only for the triaxiality values over η_1 . From η_1 to η_2 the shear damage effect is linearly reduced whereas after η_2 it is completely eliminated. Nielsen and Tvergaard (2009) proposes two possible correction intervals, (η_1, η_2) , as (0, 0.5) and (0.2, 0.7). It should be noted that both shear modifications of Nahshon and Hutchinson (2008) and correction terms of Nielsen and Tvergaard (2009) have strong effects on the evaluation of damage accumulation in plane strain bending. Following Nahshon and Hutchinson (2008) for plane strain states, where $\eta \approx 0.577$, shear damage growth to is fully active since $w \approx 1$. With the presented corrections, for the interval (0, 0.5), one has $w = 0$ and for (0.2, 0.7) one has $w \approx 0.244$. For the former case shear modification is completely suppressed, whereas for the latter case it is reduced nearly to one fourth. As noted earlier due to the hydrostatic stress dependence of the yield function as opposed to the Levy–Mises flow rule current framework results in a dilatant plastic flow. Accordingly the stress triaxiality ratio is not necessarily constant for constant strain paths where deviations depend mainly on the level of porosity and hydrostatic stress. Since for the high strength steel sheets initial porosity is considerably small, deviation of the stress triaxiality under constant strain paths (in which damage development is due) become dominant only at latter stages of loading.

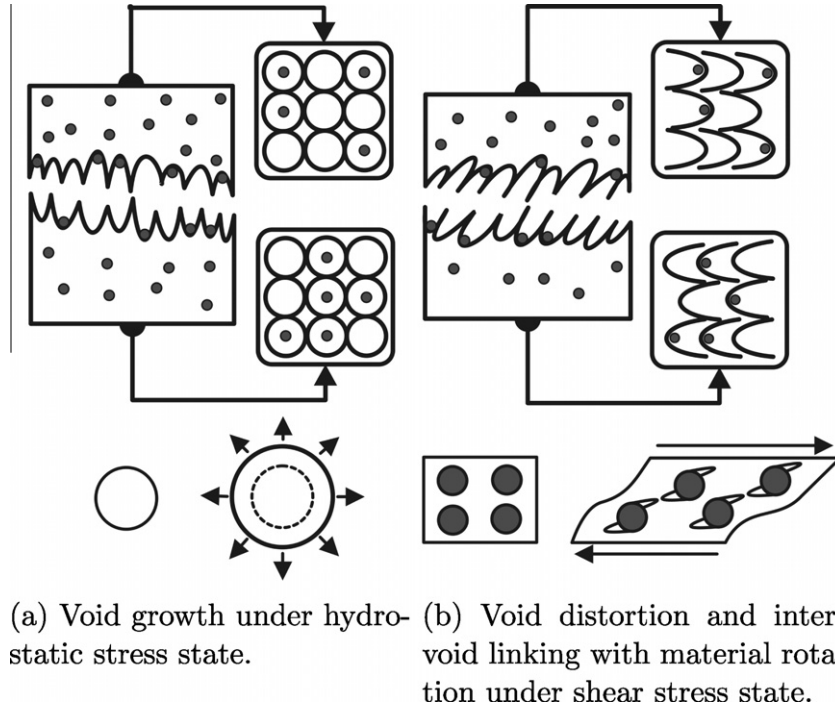


Fig. 1. Damage development under different stress states and characteristic fracture surface evidences.

This concludes the theoretical background regarding the shear modified Gurson's damage model. Eventually, the complete set of equations to be solved reads

$$\left. \begin{aligned} \partial_t \mathbf{E} &= \partial_t \mathbf{E}^e + \partial_t \mathbf{E}^p, \\ \partial_t \mathbf{T} &= \mathbb{C}^e : \partial_t \mathbf{E}^e, \\ \partial_t \mathbf{E}^p &= \dot{\gamma} \partial_t \Phi^p, \\ \partial_t e^p &= \dot{\gamma} \eta : \partial_t \Phi^p, \\ \partial_t f &= \dot{\gamma} [A_N \eta + \mathbf{B}_G] : \partial_t \Phi^p. \end{aligned} \right\} \quad (12)$$

where $\eta := \mathbf{T} / [(1-f)\sigma_y]$. In above the evolution of void growth is shortly represented as

$$\partial_t f^G = \mathbf{B}_G : \partial_t \mathbf{E}^p \quad (13)$$

where the second order operator, \mathbf{B}_G , is defined as

$$\mathbf{B}_G = \mathbf{B}_G(f, \text{dev}[\mathbf{T}]) = (1-f)\mathbf{1} + k_w f \frac{w(\text{dev}[\mathbf{T}])}{\sigma_{eq}} \text{dev}[\mathbf{T}]. \quad (14)$$

Using the definition of the plastic flow one can add up the damage contributions to end up with the following expression

$$\partial_t f = \dot{\gamma} \left(A_N \frac{\mathbf{T}}{(1-f)\sigma_y} + \mathbf{B}_G \right) : \partial_t \Phi^p. \quad (15)$$

An algorithmic treatment of the given framework is enclosed in the appendices.

3. Experiments

Free bending (or air bending) is a widely used brakebending operation where the blank is supported at the outer edges without being forced into a female cavity (as opposed to die bending). Thus, the bending angle is determined by the ramstroke, not by the die shape, see Kobayashi et al. (1989). This reduces the force demand for forming. However, at the same time it gives rise to free surface cracks and, if not, to relatively high springback. An analysis of springback is beyond the aim of this study. In the following, first the chemical composition and the microstructure of the utilized

material are given. Then, the experimental setup and outcomes of the tests are explained.

3.1. Chemical composition and microstructure observation of DP1000 steel

The investigated sheet material used within the scope of this work is a cold-rolled ferritic–martensitic steel, so-called DP1000. In order to figure out the chemical compositions, a chemical analysis with Optical Emission Spectroscopy (OES) is carried out. The results are summarized in Table 2.

The slag morphology as well as the amount and the size of slag inclusions were assessed using the slag inclusion evaluation method. Important information regarding inclusion quantity and size is depicted in Fig. 2.

Energy dispersive spectrometry analysis showed that the inclusions consisted mainly of manganese sulfide or calcium aluminate. Despite the fact that the cracks usually initiate near complex macro slag, in this case manganese sulfide or calcium aluminate, the martensitic islands act as potential microvoid initiation zones, respectively. Especially for ferritic–martensitic steels consisting of relatively brittle martensite surrounded by ductile ferrite, this idea gains more importance.

3.2. Experimental setup

Air bending tests are realized on universal testing machine, type Zwick 250. With reference to Fig. 3, the radii of the punch, r_p , and the dies, r_d , are 1 mm, whereas the die width, d_d , is 24 mm. The sheet has a length of 100 mm, b , a width of 50 mm, w , and a

Table 2
Chemical composition for DP1000 in wt.%.

C	Si	Mn	P	S	Cr	Ni	Al	Co
0.161	0.499	1.546	0.011	0.002	0.44	0.035	0.043	0.016

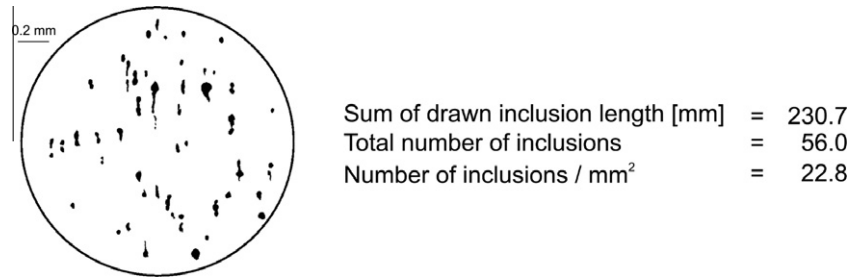


Fig. 2. Slag assessment of DP1000.

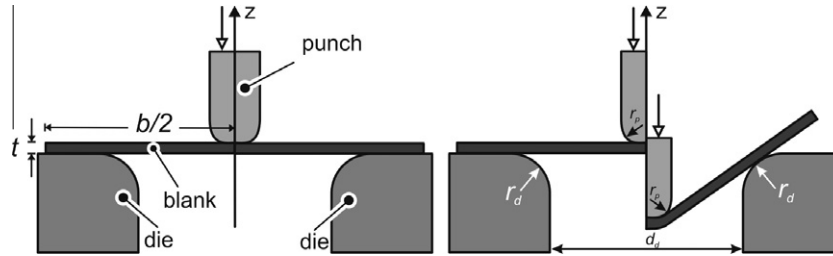


Fig. 3. Essential geometrical dimensions of the bending problem.

thickness of 1.55 mm t . The punch moves downwards while the dies are stationary.

As noted in (ASM Handbooks, 2000 [pp. 403–415]), bending occurs at plane strain conditions at $w/t > 8$, where $\epsilon_2 = 0$ and $\sigma_2/\sigma_1 = 0.5$. If $w/t < 8$, bending occurs under plane stress conditions with $\sigma_2/\sigma_1 < 0.5$ and plasticity occurs in all principal directions. For the former bend ductility is independent of the width-to-thickness ratio, whereas for the latter, bend ductility strongly depends on this ratio as given in Fig. 4. Generally, tests are performed in width-to-thickness ratios larger than 8 to 1. In the current case the width-to-thickness ratio is $w/t = 35.48 > 8$, where the plane strain assumption is validated.

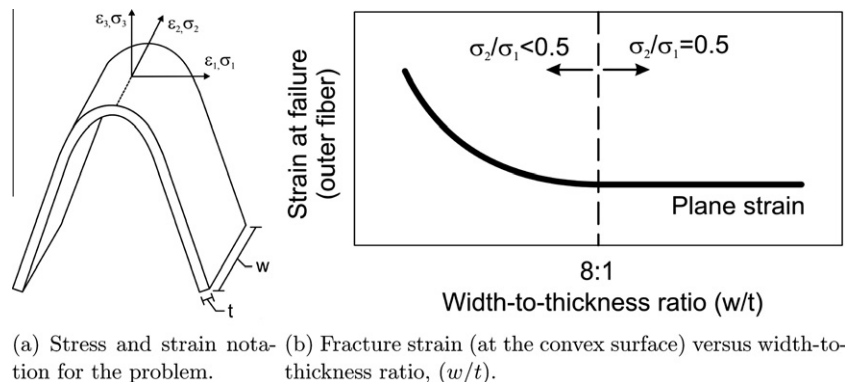
3.3. Observations at macroscale

The experiments carried out until a fracture on the convex surface of the specimen was observed. The emanation of cracks is observed at the central portions where the plane strain effect is higher rather than at the edges in accordance with the definitions given in (ASM Handbooks, 2000 [pp. 403–415]). Fig. 5 show bent specimens at different stages of the ram-stroke.

According to the test evaluation procedure presented in (ASM Handbooks, 2000[pp. 403–415]), surface examinations for cracks

are conducted on the convex surface with magnifications up to 20X where surface wrinkles or orange peeling are not considered as unacceptable defects. Fig. 6 shows the stages of cracking at the apex of the bend. With a growing extent of deformation orange peels and accompanying slight surface waviness (so-called undulation) is observed on the outer surface in the bending zone in the form of bulges and dents (or extrusions and intrusions). As explained in Dao and Lie (2001), these grooves increase the strain and plastic flow inhomogeneity at the micrometer scale and the deformation is confined to narrow localized slip bands. In general, these slip bands, act as sources of extrusions and intrusions when intersect a free surface. Cracks emanate from intrusions, which is in correlation with the observations made in bending where the intruded portions of undulations (or waviness) are the crack emanation zones.

These outcomes are in accordance with those obtained by Sarkar et al. (2001), where observed phenomena of bending defects in AA5754 Al alloys for low and high Fe content are listed as: (1) Strain localization at various length scales, (2) Undulations at the surface, (3) Damage acceleration in localization bands in Fe rich microstructures, which are linked to surface grooves and fracture occurs inclined to the surface. The sequence and relation of these events are linked to a second phase particle content (Fe), where



(a) Stress and strain notation for the problem. (b) Fracture strain (at the convex surface) versus width-to-thickness ratio, (w/t).

Fig. 4. Problem of bendability (adapted from (ASM Handbooks (2000)[pp. 403–415])).

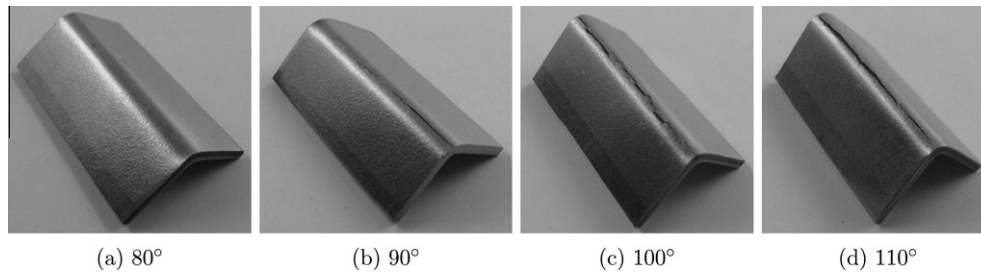


Fig. 5. Bent specimens for different levels of deformation measured in terms of bending angle.

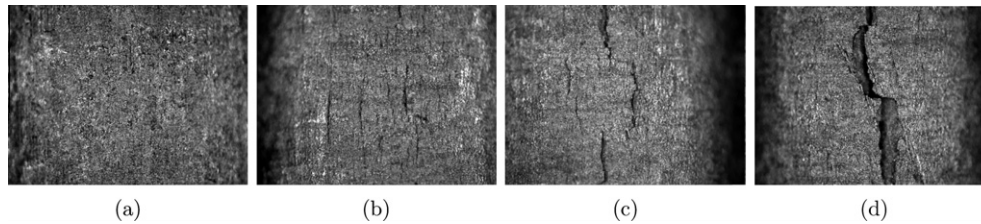


Fig. 6. Development of surface undulations by the extent of deformation.

the degree of material inhomogeneity and spacing of particles gain importance. Accordingly, small interparticle spacing in high Fe alloys promotes the linking of voids where the failure occurs in the form of void sheeting. It is shown that high Fe alloys show lower bendability. Cavity formation in the particles interacting with slip lines under the influence of shearing is clearly shown by SEM images. It is also shown that the prestrained materials show lower strain hardening rates, under loading due to their decreased hardening capacity; thus, undulations and associated localizations occur earlier, which initiates a softening effect again. Lievers et al. (2003a) investigate the bendability of AA6111 sheets for different Fe concentrations using a combined experimental numerical procedure.

Crack alternation at the bend apex is shown in Fig. 7. As will be further clarified by means of a section analysis and post-mortem surface fractographs, phenomena like alternating cracks at the apex along the central bending line, incipient cracks under free surface, crack trajectories, i.e. the size and orientation of crack tip evolution are strongly linked to the local material inhomogeneities. Our observations show that the cracks tend to alternate from one localization band to another under the effect of cavitation, i.e. inclusion type, size, shape, and distribution. Once the local inhomogeneities are insufficient, the post-mortem fracture surfaces show less clues regarding parabolic dimples, which shows that plastic slip mechanisms dominate compared to void sheet mechanisms. Thus, the cracks alternate from a less critical localization

condition to a more critical one, following maximum damage paths, comparable with the observations of Sarkar et al. (2001) where it is detected that damage accelerates in localization bands in inclusion rich (Fe) microstructures.

Once the crack paths at random sections orthogonal to the bending axis, as seen in Fig. 8, are analyzed, three characteristics are observed: (1) It can be noted that when the bending axis is orthogonal to the rolling direction cracking at the outer fiber occurs later than in transverse direction due to elongated inclusions, also noted in (Meyers and Chawla, 2009 [p. 233]). (2) The cracks emanate from the free surface along the slip bands with maximum plastic straining at an angle of approximately 45° to the principal stress direction which is due to the tension of the outermost fiber. This structure is compatible with a combined Mode I Mode II fracture where the opening and shearing modes act. (3) After the cracks have reached a certain length they change direction to form a zig-zag pattern.

For a transgranular brittle fracture a slight zig-zag pattern can be handled with the crack arrest at grain boundaries where the preferred splitting plane from grain to grain may differ in orientation, resulting in faceted fracture surfaces. For the current ductile pattern this may be attributed to a blending of two alternative mechanisms:

(Broek, 1982 [p. 13]) links this behavior to the bimodal particle distributions. Localized deformations in the form of shear bands occur between large particles which generally break or get loose

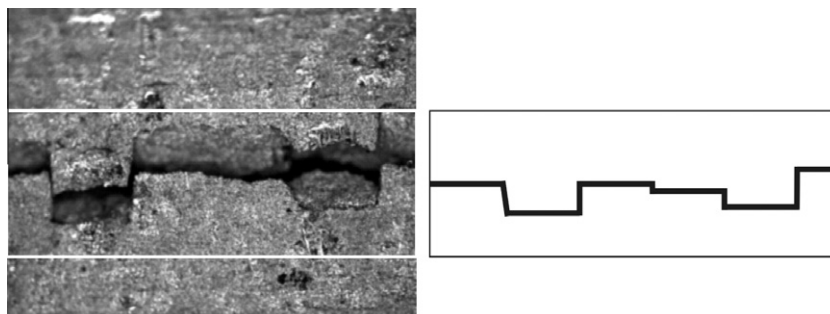


Fig. 7. Crack alternation along the bending axis at the bend apex.

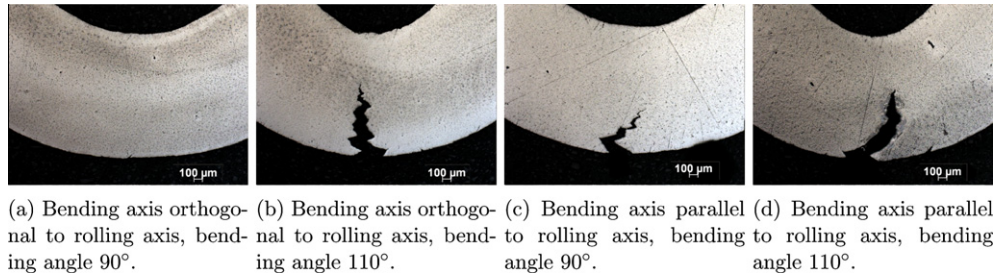


Fig. 8. Observed crack patterns on the bend section.

earlier to form widely spaced holes in the vicinity of the crack tip. These join up by void linking and shearing through micro-void coalescence in smaller secondary particles. Accordingly, the crack changes direction in between the large particles. Due to this mechanism, the fracture surface includes both the dimples of smaller and larger particles.

According to Anderson (2004), any crack subjected to Mode I loading tends to propagate through the preferred path of void coalescence which is the maximum plastic strain i.e. plastic localization path at 45° to the principal tensile stress. This determines the crack direction at the local level, whereas the global constraints tend to hold the crack on the plane orthogonal to the maximum stress. The resulting conciliatory path has a zig-zag pattern. These observations are in accordance with similar ideas proposed in Beauchem and Yoder (1973) which, while investigating zig-zag ductile fracture patterns in the form of periodic ridges and valleys, link the size of ridges and valleys to fracture toughness.

Finally, the average punch force-punch displacement curve is given in Fig. 9 since the material does not have strong anisotropy, Malekipour Gharbi et al. (2011). No large gap in between the level of maximum forces for specimens bent at different orientations (0° and 90°) with respect to their rolling directions is observed. Comparisons with the simulations are stated in the following sections.

3.4. Observations at microscale

Surface fractography is a powerful tool when determining the character and type of fracture. In the following, we summarize post-mortem surface fractography analyses by SEM with different magnifications as evidence for ductile fracturing mechanisms which occur under the influence of intense localization with void sheeting.

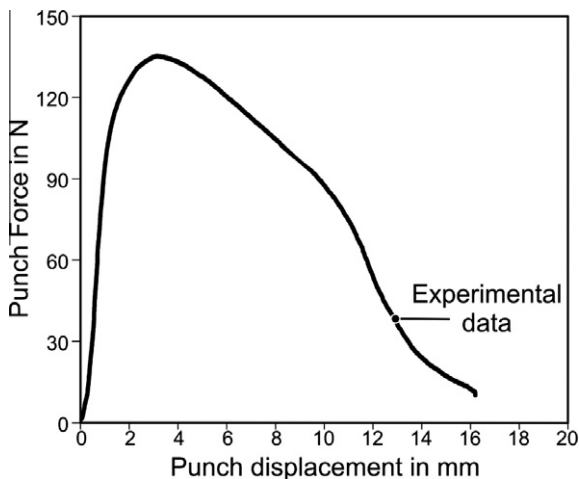


Fig. 9. Experimentally handled load-displacement curve for the punch.

Fig. 10(a) shows the region where the SEM analyses are conducted. The upper free surface shows the apex of the bend. In general, the dimple formations at the fracture surface constitute a clear sign for the ductility of fracture. However, the surface features are relatively complicated, so the analysis is divided into certain regions. We concentrate on two regions, mainly where Fig. 10(b) (namely region A2) shows the fracture surface in the vicinity of crack emanation at the free surface at the bending apex and 10(c) (namely region A6) shows a relatively inner region closer to the neutral axis of the bend.

Region A3 is divided into two finer scale regions, namely region A4 and A5, for dimple pattern observations, as seen in Fig. 11. Region A5 is closer to the crack alternation zone, whereas region A4 is relatively remote from this region. A5 shows relatively flat surface characteristics where the shearing direction is slightly oriented towards to a possible effect of crack alternation. As opposed, region A4 includes more obvious dimples forming a relatively rough surface where the shear loading has, as expected, a vertical direction. In both A4 and A5 the type of dimples is parabolic which shows the slantness of the fracture surface, see e.g. (Hull, 1999 [p. 238]), where the Mode II fracture is dominates among a blended Mode I and Mode II type fracture. The local change of fracture surface characteristics, such as increased surface flatness and reduced parabolic dimples in the vicinity of crack alternation, might be responsible for the crack's bifurcation into a less stiff or more developed localization band.

Fig. 12 shows the surface features observed in region A6 with a finer scale SEM fractograph, which gives A7, and a further refined region A8. These coincide with the region where crack zig-zagging occurs. An evident observation is the relatively coarse surface characteristics compared to region A2. In region A7 the dimples are more remarkable and a blend of larger and smaller dimples is observed. As seen in more detail in region A8, the dimple types are still parabolic. Again, the shear loading is dominant and the direction of loading is apparent from the fractographs.

4. Simulations

The presented theoretical framework is implemented into VU-MAT subroutines for ABAQUS/EXPLICIT where the algorithmic forms can be found in the appendices. Simulations are conducted in both 2D plane strain and 3D with double precision. A solution of quasi-static problems with a dynamic-explicit solution procedure generally involves a very large number of time steps. In order to reduce the computational cost, mass scaling is applied with a target time step of $2.5e-7$ over the whole analysis. Based on the statics of all elements the mean stable time increment estimate without mass scaling is $3.0e-9$. Accordingly, the mass scaling applied corresponds to nearly $1.0e4$. On this rather conservative selection local integration method based on cutting plane algorithms was also conclusive. The material has a modulus of elasticity, E , of $E = 210000$ MPa and the Poisson's ratio, ν , is

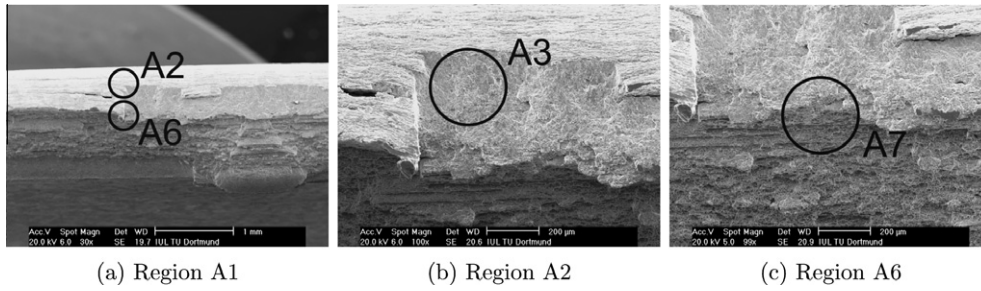


Fig. 10. SEM fractographs from fracture surfaces, Part I.

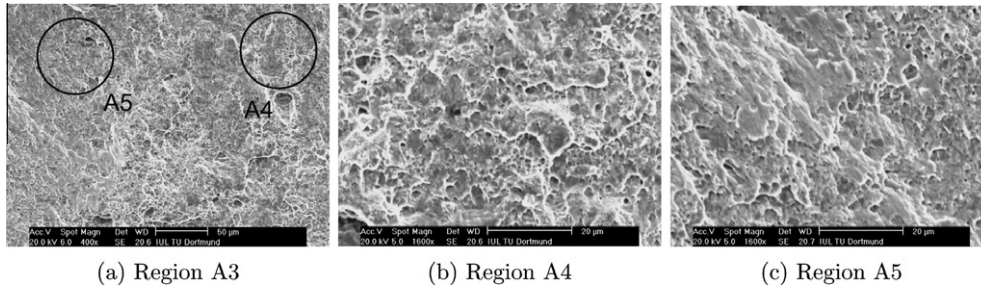


Fig. 11. SEM fractographs from fracture surfaces, Part II.

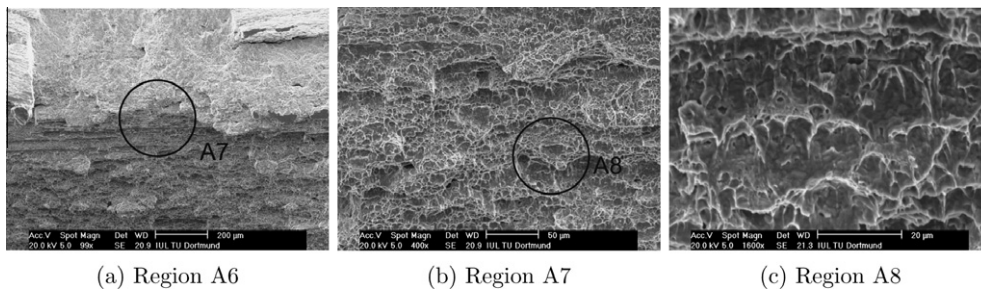


Fig. 12. SEM fractographs from fracture surfaces, Part III.

$\nu = 0.3$. The hardening curve is constructed by fitting data until the necking point and using extrapolation for the post-neck. The extrapolated flow curve is given in Fig. 13. The anisotropy due to the rolling process is not taken into account.

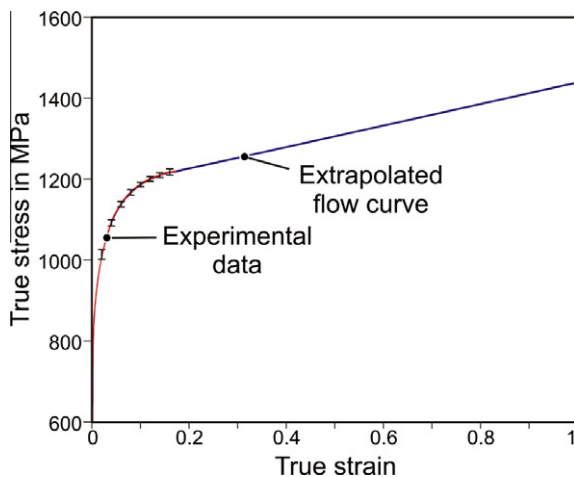


Fig. 13. Flow curve for DP1000.

It is desirable that a chemical analysis and/or quantitative metallography is used in order to estimate the initial porosity where constituents dominating the ductile fracture mechanism by acting as damage nucleation sites are taken into account, Jackiewicz (2009). The Franklin's formula, Franklin (1969), serves as an estimate for f_0 where manganese sulphide inclusions are the critical particles in fracture:

$$f_0 = \frac{0.054 \sqrt{d_x d_y}}{d_z} \left(S(\%) - \frac{0.001}{Mn(\%)} \right), \quad (16)$$

where d_x , d_y , and d_z denote average inclusion diameters in the respective directions. $S(\%)$ and $Mn(\%)$ represents the weight percentages of sulphide and manganese in the matrix. Details on the usage of this relation can be found in Franklin (1969). Since this form relies on the quantitative metallography of materials where manganese sulphide inclusions dominate the fracture, a modification for the case of advanced high strength steels (DP, CP, and TRIP) is required implying a combined effect of inclusions and secondary phases on fracture. In DP steels hard martensitic islands have 5–20 vol% which controls the ultimate tensile strength. Typical compositions of cold-rolled DP steels involve (wt.%) 0.08–0.15% C, 1.6–2.2% Mn, 0.4% (Cr + Mo) (Meyers and Chawla, 2009[p. 590]). So this procedure is not followed.

In this class of steels the void nucleation depends on the non-metallic inclusions ($\sim 5\text{--}30\ \mu\text{m}$ in diameter) as well as dispersed martensite particles ($\sim 0.5\ \mu\text{m}$ in diameter), see e.g. Tasan (2010). Accordingly, the orders of magnitudes of respective particle sizes differ. The volume fraction shows an opposing trend where non-metallic inclusions constitute 0.01–0.05 vol%, whereas martensitic islands reach 5–20 vol%. Experimental investigations of Poruks et al. (2006) show that void nucleation at inclusions, either with particle cracking or inclusion-matrix decohesion, occurs at relatively low strains (~ 0.2) due to pre-existing cracks and weakly bonded interfaces. In comparison, the void nucleation strain is higher (~ 0.9) due to a relative coherence of the ferrite-martensite interface at martensite particles. It is noted that the fracture is controlled by growth and coalescence of martensitic void nucleation sources which is attributed to the higher volumetric fraction of martensite compared to non-metallic inclusions.

For the base shear enhanced Gurson parameters reported values in the literature are followed where in the analysis the effect of variations of certain ones are also investigated. These are summarized in Table 3. The parameters q_1, q_2, q_3 are chosen following Tvergaard (1981, 1982a). Nielsen and Tvergaard (2010) and Betttaieb et al. (2010) use similar parameters for the Gurson's damage model for DP600 and DP1000, respectively. f_c and f_F are selected following Andersson (1977), Brown and Embury (1973), Nahshon and Xue (2009). k_w is selected as 2 which lies in the proposed range for structural alloys, $1 < k_w < 3$, Nahshon and Hutchinson (2008). Selected f_0 is also due to Betttaieb et al. (2010). For f_0, f_c, f_F and k_w a parametric study is also followed to investigate their relative effects on localization and fracture.

4.1. 2D Plane strain models

Plane strain state is assumed. The dies and the punch are modeled as rigid curves, whereas the blank is modeled as a deformable body, as seen in Fig. 14. In the following, a set of sensitivity analyses which investigate the effect of process parameters on localization, crack pattern, and load–displacement curves are summarized.

4.1.1. The effect of mesh size

Capturing correct deformation and localization patterns requires fine meshes as noted by Becker and Needleman (1986), on modeling cup-cone fracture mode in axisymmetric tension, see also Tvergaard and Needleman (1984). In bending, highly inhomogeneous plastic flow localization is observed at micrometer scales until crack occurrence. In order to capture the size of localization or the physical crack size, we start by testing three different mesh refinement levels at the bend region which are 0.04 mm, 0.03 mm and 0.02 mm, see in Fig. 15(a)–(c), respectively, for the selection of a proper mesh size at the bending region. The total number of elements is, as a consequence, 5265, 7017 and 10767, respectively, using CPE4R, i.e. 4-node bilinear plane strain quadrilateral, reduced integration elements with hourglass control. It is noteworthy to say that once insufficiently refined meshes are supplied, the physically observed inclined localizations and cracks are not captured properly. The mesh is also refined in the contact regions in the vicinity of the dies for a smooth node to surface contact treatment. Otherwise large scatters on the punch force–displacement diagram can be observed.

Resultant damage distributions prior to crack occurrence are given in Fig. 16. The mesh dependence of localization is seen in

the plots where the localization bands occur with an orientation of approximately 45° with respect to the principal stress direction. The time of localization, number of localization bands, and the damage intensities within the bands differ for each mesh. As noted by Tvergaard (1987), the results admit a length scale where a strong mesh dependence occurs. For smaller element sizes narrower localization bands are carried out. Moreover, the localization occurs earlier. A finite band width is enforced in materials by involving of inherent length scales, such as grain, inclusion, or void size. A natural length scale which limits the banding is not supplied in conventional continuum mechanics formulations. In finite element simulations, when not explicitly involved, the element size acts as a length scale. Accordingly, a general trend in literature is to use the mesh size as a material parameter and to fix it during the material characterization phase. More general methods, named nonlocal approaches, involve an explicit definition of the length scale, which falls beyond the aim of this study.

The cracks are modeled using element deletion technique which serves as a standard procedure of ABAQUS/EXPLICIT. Accordingly, the reduced integration elements, whose Gauss point's damage value reaches f_f , are excluded from the computational stack. Element deletion technique is also used in Wisselink and Huetink (2007, 2008, 2009). Similar methods are used in Tvergaard (1982a, 1987), and Lievers et al. (2003b) where a final fracture is created by a progressive stiffness and strength degradation, the so-called crack smearing technique. Resultant cracks, which occur with bifurcation into one of the developed bands, are given in Fig. 17 for identical punch displacements. The size of the cracks change with the mesh size. For the mesh with 0.04 mm element size the crack is not developed yet due to an insufficient damage development, whereas for 0.02 mm element size the crack initiates. For both 0.03 mm and 0.02 mm meshes the cracks change direction after a certain crack length. Although this is attributed to different micro-mechanical phenomena, as explained earlier, in the simulations the results can be ascribed to overlapping localization patterns and macroscopic loading conditions which force the cracks to stay on the symmetry axis.

The punch force–displacement curves are given in Fig. 18. The points of steep decrease at the load levels are the incipient cracking points. In accordance with the localization analysis the loss of load carrying capacity is first observed in the model with the finest mesh. Prior to this cracking point no remarkable difference is observed in the load displacement diagrams. This may be attributed to the fact that until the fracture occurrence with localization the damage values reached are relatively small in magnitude and the damage spread only appears as a small scale phenomenon. Eventually, its distribution throughout the section of interest is limited in both intensity and extent.

The damage over the bend region, which reaches a maximum at the convex surface to create localization, is formed by three contributions, namely void nucleation, damage growth due to triaxiality, and damage growth due to shear. Fig. 19 shows the individual distributions of these components for the analysis with 0.030 mm mesh size at an intermediate analysis step. Since void nucleation is assumed not to occur under negative hydrostatic stress states it acts only at the tensile portion below the neutral axis. On the convex surface however at this level of deformation all void nucleation source, which is 0.020, is reached. Coming to damage growth, we see a maximum growth at the convex surface as anticipated. On

Table 3
Base Gurson's parameters for DP1000.

$q_1 = 1/f_0$	q_2	q_3	f_0	f_N	s_N	ϵ_N	f_c	f_F	k_w
1.500	1.000	2.250	0.002	0.020	0.110	0.350	0.150	0.250	2.000

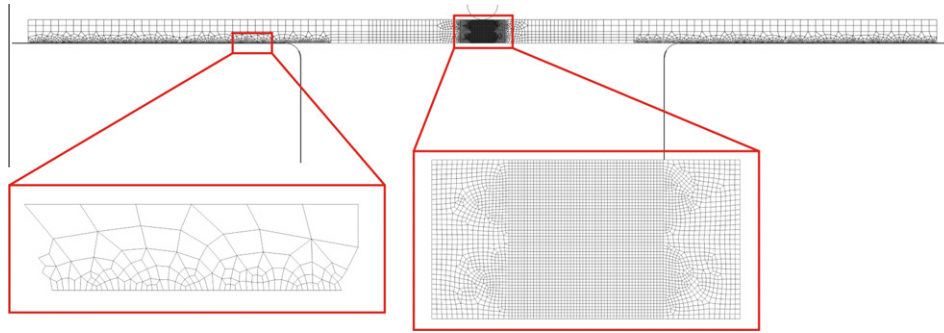


Fig. 14. 2D plane strain model for free bending.

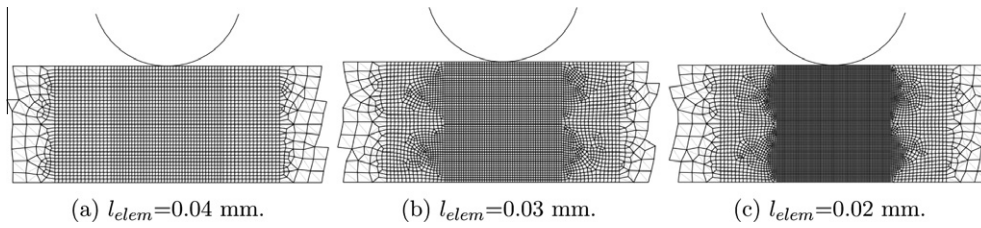


Fig. 15. Mesh refinement in the bending region for the 2D model.

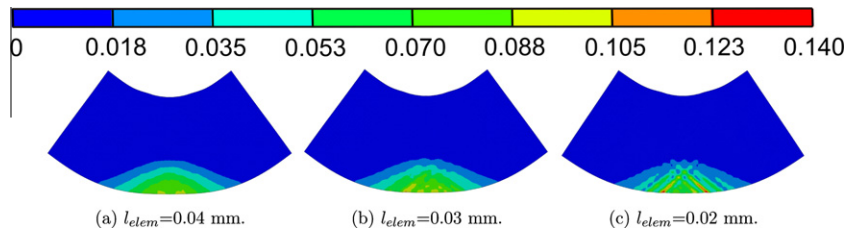


Fig. 16. The effect of mesh size on damage localization, punch displacement = 10.2 mm.

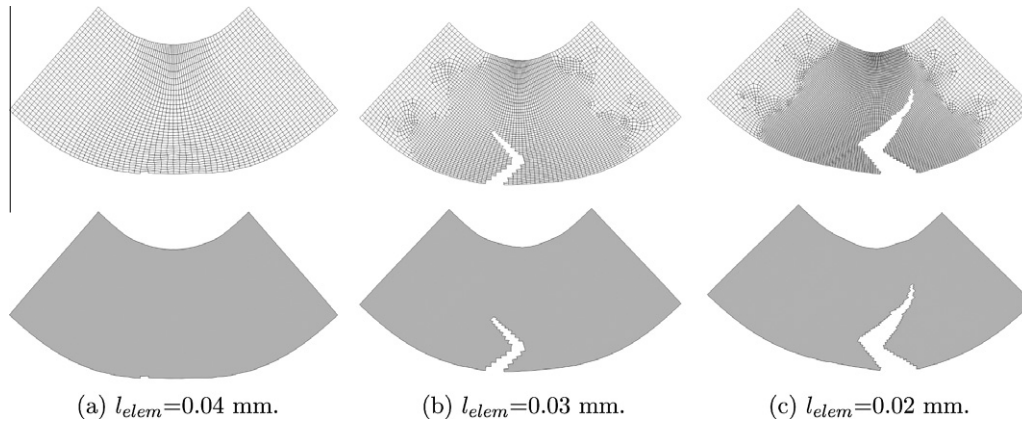


Fig. 17. The effect of mesh size on fracture pattern, punch displacement = 13.0 mm.

the concave surface damage reduction (in classical terminology this corresponds to void shrinkage) is observed with an absolute maximum value in the region which is in contact with the punch.

Fig. 20 shows that damage growth due to shear is in the same order of magnitude as the damage growth due to triaxiality at the convex face. This is primarily due to the previously mentioned plane strain constraint which supplies $w \approx 1$. A relatively large triaxiality ratio $\eta \approx 0.577$ creates the hydrostatic stress-dependent void growth. Although damage growth due to shear occurs at the

concave face and above the neutral axis it does not suffice to overcome damage reduction due to a compressive hydrostatic stress state to give $f^g < 0$. Under these conditions, a ductile damage mechanism with growth of voids is not possible at the concave surface, which is in correlation with the proposed fracture cut-off triaxiality as $\eta = -1/3$, Bao and Wierzbicki (2005), since at the concave free surface, plane strain compression results in $\eta \approx -0.577$ whereas under the punch this reduces further due to compressive contact loads.

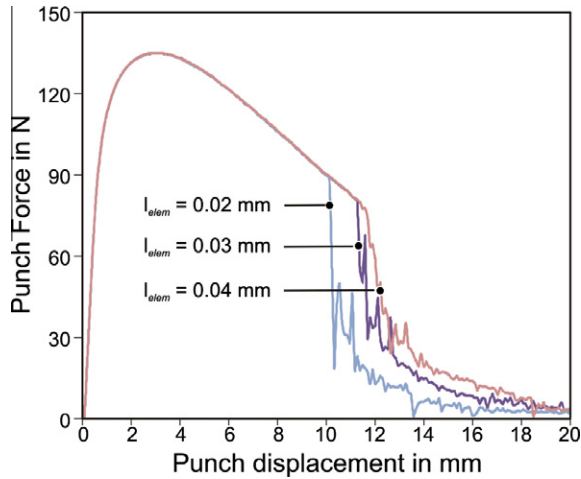


Fig. 18. The effect of mesh size on force–displacement curves.

The authors' experience shows that once the initial porosity is taken as $f_0 = 0$ the compressive region above the neutral axis experiences no damage evolution, although shear damage growth might be expected due to the underlying physical mechanisms. This stems from the combined conditions where (1) the void nucleation requires a positive hydrostatic stress state, (2) already precluded damage reduction (void shrinkage) with completely eliminated porosity, and (3) the necessity of shear damage growth for an initial damage, which is seen from its evolutionary equation. Once an initial non-zero porosity is supplied, the current formulation gives rise to both void shrinkage due to negative triaxiality and damage growth due to shear. The summation of the damage growth rate may be negative, as it is seen in the current problem, depending on the loading conditions which will be a statement of void shrinkage beyond initial porosity. With an alternative formulation, Besson (2009) proposes the following modified potential

$$\hat{\phi}^p = \left(\frac{\sigma_{eq}}{\sigma_y} \right)^2 + 2q_1 f^* \cosh \left[\theta \frac{3}{2} \frac{q_2 \sigma_m}{\sigma_y} \right] - (1 + q_3 f^{*2}) = 0, \quad (17)$$

where

$$\theta = \begin{cases} 1 & \text{if } f^g > 0 \text{ or } \sigma_m \geq 0 \text{ and} \\ 0 & \text{if } f^g = 0. \end{cases} \quad (18)$$

which supplies $f^g \geq 0$ even for negative hydrostatic stresses. This approach, also used by Bettaieb et al. (2010), clearly hinders void shrinkage beyond initial porosity. This, of course, affects the damage evolution at the concave free surface of the bend and the compressive region above the natural axis.

4.1.2. The effect of k_w

For the following studies, the mesh size is selected to be 0.03 mm due to the correlation in between experimentally and numerically captured fracture time and size as well as the computational cost. Fig. 21 shows the damage distributions and deformation localization patterns for various k_w values. At identical step sizes, loss of adequate softening results in no localization for $k_w = 0$ and $k_w = 1$. In the current simulations a sufficient damage accumulation for localization with softening is around %10–%15. For $k_w = 2$ and $k_w = 3$ one observes well-developed deformation bands.

Fig. 22 gives crack paths for an identical ram stroke. For $k_w = 0$ and $k_w = 1$ no cracks are developed yet. For $k_w = 2$ and $k_w = 3$ there are crack occurrences when the crack size depends on k_w . This is anticipated since k_w controls the damage accumulation till fracture. Crack kinking is observed in both of the cases as well for which similar comments made for the mesh size effect apply.

The punch force–displacement curves are given in Fig. 23. As it can be seen the earliest loss of load carrying capacity is observed for $k_w = 3$, whereas for $k_w = 0$ and $k_w = 1$ no steep decrease arises since no crack occurrence is captured within the selected loading interval. There is only a slight difference between the curves with different k_w values.

A comparison of the force–displacement curves for $k_w = 2$ and $k_w = 3$ with experimental data is given in Fig. 24. The simulation results agree qualitatively with the experimentally investigated ones for $k_w = 2$. The unloading portions in the plane strain analysis give a steeper drop compared to the experimental results in which the overall section is not cracked, but the crack gradually propagates from the central plane strain regions to the edges. We further comment on this issue in the 3D model simulations section.

4.1.3. The effects of f_0, f_c , and f_f

A set of analyses is run for different values of f_0, f_c , and f_f . The results are summarized in Fig. 25. In correlation with the findings of Lievers et al. (2003b) inclined crack patterns are only considered

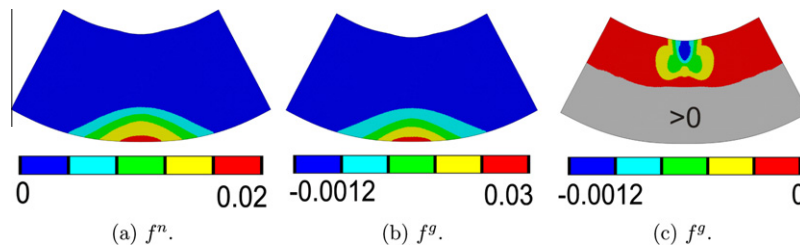


Fig. 19. Individual contributions of damage components in the bend region, punch displacement = 8.0 mm.

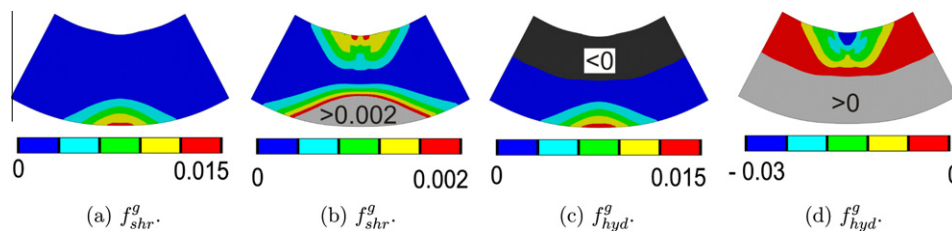


Fig. 20. Individual contributions of damage growth components at the bend region, punch displacement = 8.0 mm. As respectively seen in (c) and (d) there is negative damage growth (i.e. damage reduction) above neutral axis and positive damage growth below neutral axis.

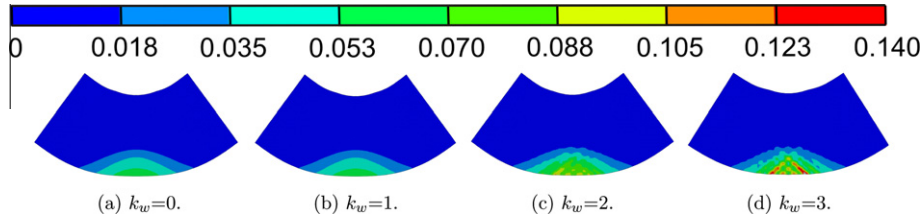


Fig. 21. The effect of mesh size on damage localization, punch displacement = 10.2 mm.

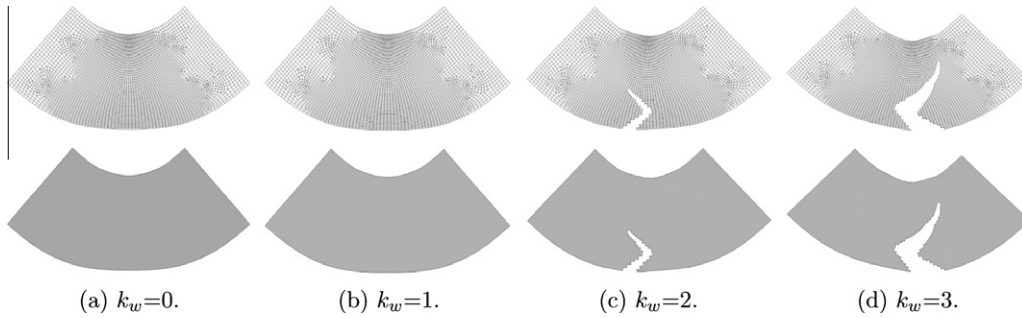


Fig. 22. The effect of k_w on fracture pattern, punch displacement = 13.0 mm.

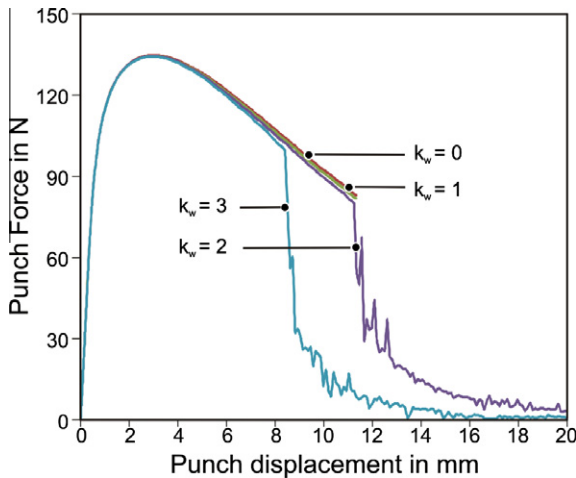


Fig. 23. The effect of k_w on force-displacement curves.

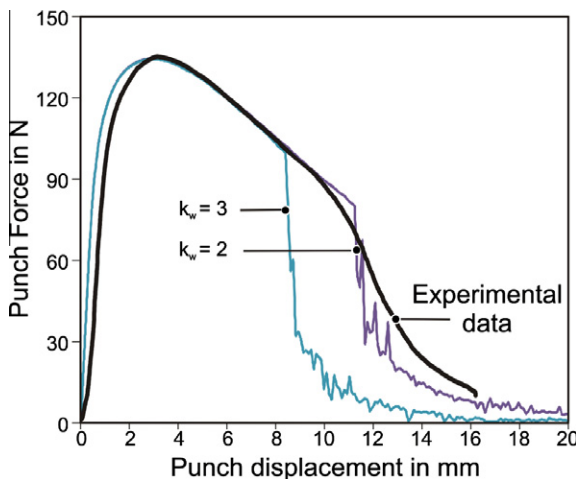


Fig. 24. Comparison of experimental and numerical (2D plane strain) force displacement curves.

when the incipient crack is accompanied by a localization band. As seen in Fig. 25(c) and (d), once the critical limit for coalescence and final fracture is kept too low, the crack emanates at the center and propagates orthogonal to the maximum principal stress direction as it is in the case of tensile stress controlled cleavage-type brittle fracture. However, in the current case plastic flow is the driving mechanism together with tensile stress, although the fracture occurs at relatively smaller fracture strains. Fig. 25(a), (b), (e) and (f) shows the effect of initial void volume fraction on the final fracture patterns for the same punch displacement where f_c and f_f are kept constant. As seen large f_0 gives account for an accelerated damage development at successive loading stages which finally results in earlier fracture. Additionally, it can be seen that in general the crack experiences at least one kink and changes direction.

4.1.4. The effect of Nielsen and Tvergaard's modification

Plane strain state dominates the current bending problem for the selected width-to-thickness ratio. As mentioned before, under these conditions the shear damage effect is fully involved since $w \approx 1$, although triaxiality, $\eta \approx 0.577$, is not low. With the motivation that the original Gurson's damage model works sufficiently well for moderate to high stress triaxialities Nielsen and Tvergaard (2010) introduce an additional triaxiality-dependent scaling parameter for the shear modification which is given in Eq. 11. In this part of the study we present the effect of this correction, selecting the triaxiality correction interval as $(\eta_1, \eta_2) = (0.2, 0.7)$ which is one of the proposed intervals in Nielsen and Tvergaard (2010). As aforementioned for the other proposed interval, i.e. $(\eta_1, \eta_2) = (0, 0.5)$, shear modification will be completely suppressed for the current problem.

Fig. 26 represents the extent of modification for the bending problem. As an inherent property the region above the neutral axis experiences negative triaxialities in bending, i.e. $\eta < 0$. This region is not effected by shear correction, which can be seen in Fig. 26(c) where the correction factor is $\chi(\eta) = 1$. Coming to the tensile zone, although for Nahshon and Hutchinson's original form, $w \approx 1$ dominates the section, depending on the gradual increase of triaxiality towards the convex surface where it has a value of $\eta \approx 0.577$ due to plane strain tension conditions w gradually drops down to $w \approx 0.244$, its minimum value occurring at the free surface.

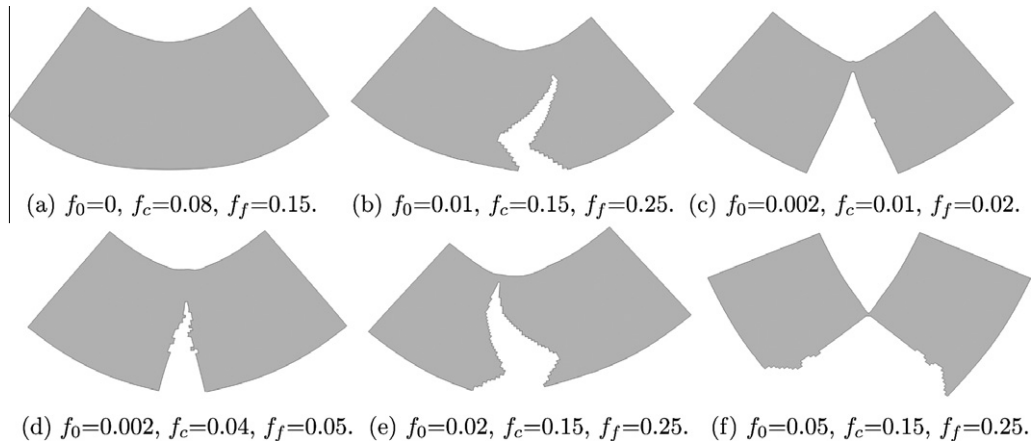


Fig. 25. The effect of process parameters on final fracture patterns, punch displacement = 11.0 mm.

In order to support the picture given in the previous paragraph, Fig. 27 shows the evolution of triaxiality over the section in the bend zone at different time steps. The triaxiality distribution over the section is close to being axis-symmetric at the initial deformation levels, whereas with the extent of deformation it involves waviness. It should be noted that the process is not a pure bending process. Above the neutral axis, negative hydrostatic stress develops which suppresses the correction effect, as seen in Fig. 26.

This modification has crucial effects on the localization behavior. Since the intensity of shear-driven damage growth drops down to a quarter of its initial value, localization does not occur in the strain range of interest. Eventually, since a developed deformation band cannot be handled, using Nielsen and Tvergaard's correction together with the selected parameter set, one cannot observe crack occurrence. These results are summarized in Fig. 28.

4.2. 3D Model

The dies and the punch are modeled as rigid surfaces, whereas the blank is modeled as a deformable body. The dies and punch radius is 1 mm. The sheet has a length of 100 mm, a width of 50 mm, and a thickness of 1.55 mm. For a reduction in computation time, half of the sheet is modeled exploiting one symmetry plane. In Fig. 29 free surface of the cross section belongs to the symmetry plane, which is also shown in Fig. 31. Mesh selection is done following the outputs of the 2D analysis. Accordingly, a 0.030 mm element size at the section bending zone is selected where the element has a relatively large aspect ratio throughout the width for computational reasons. In the die contact regions the mesh is relatively coarse compared to the 2D analysis in order to reduce time for computations. For the blank 108000 C3D8R 8-node linear brick elements with reduced integration and hourglass control are used.

4.2.1. Simulation results

Fig. 30 gives damage accumulation and consequent localization bands prior to crack occurrence. In accordance with the ASM Handbook remarks and Fig. 4, strong plane strain constraint forces incipient localization at the symmetry plane. At the edges a plane strain constraint is no longer valid and the stress mode changes to a plane stress one at the surfaces and a uniaxial one at the vertices where the η and w values reduce compared to the central portions. A gradual increase in the developed damage from the edges to the interior is seen which reaches an approximately steady state after nearly three to four thickness distance from the edges. Besides, damage distribution covers a wider area at the symmetry plane as compared to the relatively narrow distribution at the edges. Accordingly, deformation bands at the symmetry plane diffuses approaching to the edges for the same loading step. An anticlastic deformation pattern is also observed due to fibers under compression and tension at the opposing sides of the neutral axis.

The final fracture pattern is given in Fig. 31. Following the localization, an inclined crack having an orientation of approx 45° with respect to the tensile stress direction starts from the central line and propagates towards the edges. The crack direction change is clearly seen which occurs approximately at the same distance as the plane strain analysis results. The reduction of band sizes is just a consequence of this mechanism. Clearly, the crack alternation cannot be modeled in the current case. However, once an inhomogeneously distributed initial porosity is implemented, such path alternations can be anticipated due to local heterogeneity effects. Besides the effects of random porosity distribution, those of width to thickness ratio of the sheet and the strain history effects on the edge fractures are of specific importance within the reach of 3D models in bending.

As seen in Fig. 32, the load–displacement curves do not follow a sharp decrease due to gradual cracking towards the bending axis

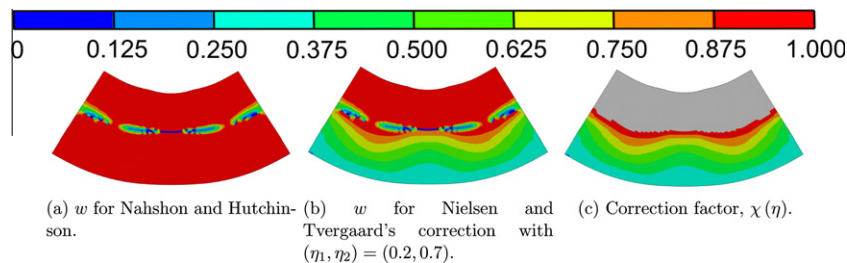


Fig. 26. Effect of Nielsen and Tvergaard's modification on w , punch displacement = 10.0 mm.

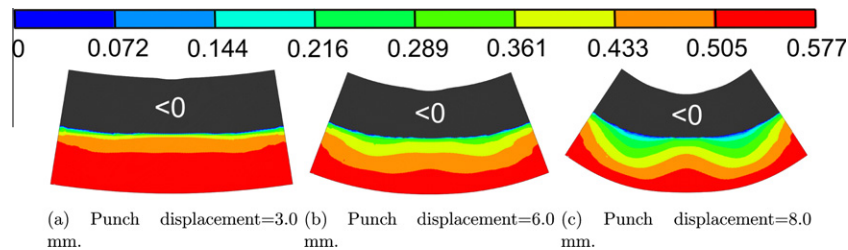


Fig. 27. The positive portion of the triaxiality distribution over the section at the bending zone.

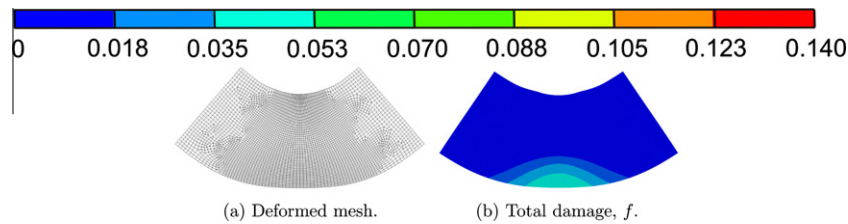


Fig. 28. Effect of Nielsen and Tvergaard's approach on damage accumulations, punch displacement = 8.0 mm, (a) Deformed mesh, (b) Total damage, f .

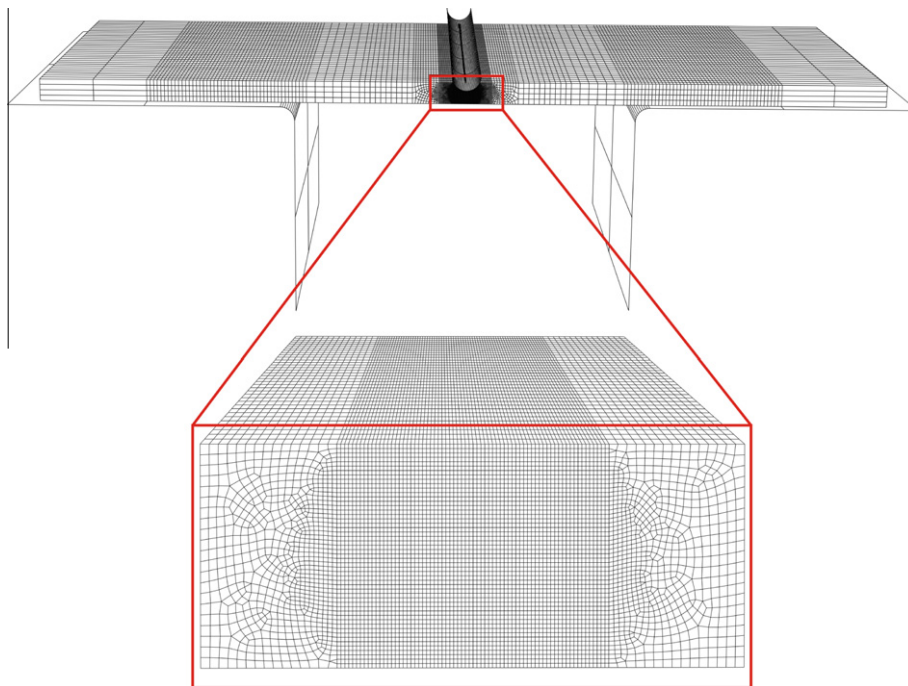


Fig. 29. 3D model for free bending. Enlarged section belongs to the plane of symmetry.

and a redistribution of load carrying capacity of the sheet. As noted before, cracks in the bent region emanate at the center and propagate to the sides. Thus, unlike plane strain simulations, the load carrying capacity progressively drops down. On the contrary, in plane strain simulations the section's load carrying capacity reduces with the occurrence of the first crack where the plane of interest represents the through-thickness plane. Accordingly, the plane strain analysis computes a steep drop of the punch force–displacement diagram. Another remark can be made on the scatters at the post-peak portion of the load–displacement curve. Unlike in the 2D analysis, these scatters are larger due to the relatively coarser mesh resolution in the contact region.

5. Conclusion and outlook

A detailed experimental numerical investigation of fracturing of DP1000 class advanced high strength steel under bending conditions is presented. Optical microscopy applied to the bend apex and cracked section and scanning electron microscopy applied to fracture surfaces show that the incipient fracture is mainly caused by cavitation and void shearing motivated strain localization. This ductile fracture mode is of a blended Mode I Mode II type. Characteristic steps such as nucleation and growth of undulations are recorded. Observations at the bend apex and various bending sections reveal that the cracks tends to alternate patterns where

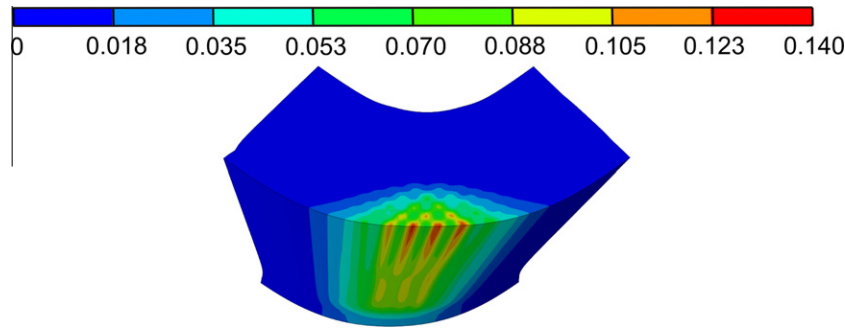


Fig. 30. Damage accumulation and localization at the plane of symmetry and the apex, punch displacement = 12.2 mm.

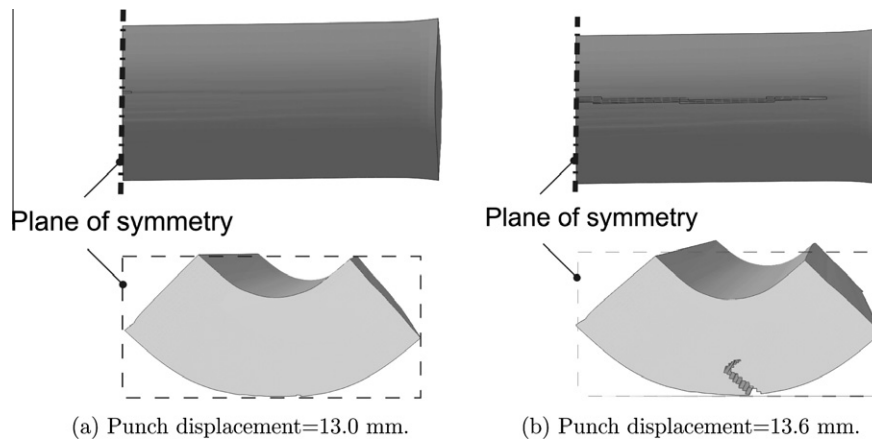


Fig. 31. Crack initiation and propagation from the central plane at the apex in 3D simulations. Top figures show the apex of the bend and bottom figures show the crack formation at the plane of symmetry.

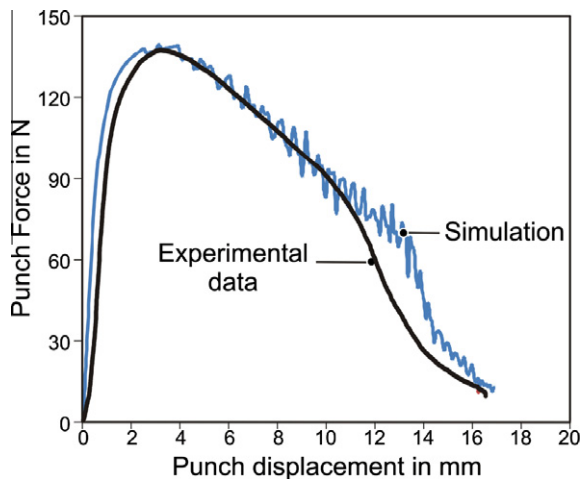


Fig. 32. Comparison of experimental and numerical (3D) load-displacement curves.

a shift from one localization band to another one is due. These are attributed to the local material inhomogeneities as well as general equilibrium requirements.

Based on these experimental evidences in the numerical analyses, Gurson's porous plasticity model is selected with recent enhancements to encounter shear-dominated failure modes. Simulations are conducted in both 2D plane strain and 3D. It is shown that 2D plane strain assumption sufficiently reflects the 3D response thanks to the sufficiently large width to thickness ratio. A detailed parameter sensitivity analysis is conducted where the

effects of mesh size, shear damage parameter, initial, critical and fracture porosities and finally the Nielsen and Tvergaard's modification on the localization and fracture patterns are investigated. It is shown that the size of the localization band is controlled by the selected mesh size which acts as an additional material parameter due to softening material response. Since the regularization of this inherent mesh size dependence is beyond the aim of this study, based on the observed localization and fracture sizes, a computationally reasonable mesh size is selected for the further sensitivity analysis. It is concluded that different variants of shear modification of Gurson's porous plasticity has direct consequences on the damage accumulation and localization deformations. This is due to the plane strain constraint inherent to the problem which indeed includes moderate triaxiality accumulation, which is around 0.577. Coming to the effect of initial porosity, critical and fracture damage values it is shown that relatively small critical damage and fracture damage parameters supply cleavage like vertical fracture patterns due to insufficient damage accumulation to localization emanation.

Acknowledgement

Financial support of C.S. for this work has been provided by the German Research Foundation DFG under Contract No. TR 73. Financial support of M.M.G. for this work has been provided by FOSTA under Contract No. P789. These supports are gratefully acknowledged. The authors thank Dipl.-Ing. Andres Weinrich of IUL (TU Dortmund) for his assistance and fruitful discussions throughout this research work. The authors also thank Dr. Björn Carlsson and Dr. Lars Troive of Svenskt Stål AB (SSAB) for their

constructive comments on the initial drafts of this study and for supplying data regarding material microstructure.

Appendix A. Kinematics of Finite Deformation Plasticity

To set the stage, particle positions at the reference (undeformed), Ω_0 , and current (deformed) configurations, Ω , respectively are denoted by \mathbf{X} and $\mathbf{x} := \boldsymbol{\varphi}(\mathbf{X}, t)$ and $\mathbf{F} := \partial_{\mathbf{x}}\mathbf{x}$ define the deformation gradient of the nonlinear map $\boldsymbol{\varphi} : \Omega_0 \times \mathbb{R} \rightarrow \mathbb{R}^3$. Any infinitesimal material vector $d\mathbf{X}$ at the reference configuration is transformed to its final setting $d\mathbf{x}$ at the current configuration via

$$\mathbf{x} := \mathbf{F} \bullet d\mathbf{X}. \quad (\text{A.1})$$

Small strain plasticity is based on the additivity of the total strain tensor into elastic and plastic portions where the computation of the stress tensor utilizes a conventional elastic stress definition. In the finite strain regimes, however, such an additivity assumption is not straightforward. Generally, finite plasticity is studied by use of two distinct approaches: namely a hypoelastic-plastic and a hyperelastic-plastic approach. The hypoelastic-plastic approach relies on the additivity of the rate of the deformation tensor into elastic and plastic portions where the computation of the stress tensor requires an integration of objective stress rates. The hyperelastic-plastic approach, on the other hand, is based on the multiplicative factorization of the deformation gradient into elastic and plastic portions where the stress is derived from a properly defined elastic free energy potential. In the following, at least in the kinematic-based section, we show that the multiplicative kinematics boils down to the rate additive form under the restriction of small elastic strains. We set the point of departure as the multiplicative kinematic split of the deformation gradient, viz.

$$\mathbf{F} := \mathbf{F}^e \bullet \mathbf{F}^p, \quad (\text{A.2})$$

which introduces an elastically unloaded plastic intermediate configuration. Let $\mathbf{I} := \partial_t \mathbf{F} \bullet \mathbf{F}^{-1} = \partial_{\mathbf{x}} \mathbf{v} \bullet \partial_{\mathbf{x}} \mathbf{X} = \partial_{\mathbf{x}} \mathbf{v}$ denote the spatial velocity gradient, with $\mathbf{v} = \partial_t \mathbf{x}$. Noting that $\mathbf{F}^{-1} = \mathbf{F}^{p,-1} \bullet \mathbf{F}^{e,-1}$ and defining $\mathbf{I}^e := \partial_t \mathbf{F}^e \bullet \mathbf{F}^{e,-1}$ and $\mathbf{I}^p := \partial_t \mathbf{F}^p \bullet \mathbf{F}^{p,-1}$ one has

$$\mathbf{I} = \mathbf{I}^e + \mathbf{F}^e \bullet \mathbf{I}^p \bullet \mathbf{F}^{e,-1}. \quad (\text{A.3})$$

For metal plasticity a fundamental observation is that the range of elastic strains falls far below the range of plastic ones. As a consequence, for metal forming processes, one assumes a small elastic strain assumption, i.e. $\mathbf{F}^e \approx \mathbf{1}$, which supplies

$$\mathbf{I} = \mathbf{I}^e + \mathbf{I}^p, \quad (\text{A.4})$$

Using the property that any tensor can be split into its symmetric and skewsymmetric portions, one has

$$\mathbf{I} = \mathbf{d} + \mathbf{w}, \quad (\text{A.5})$$

where the symmetric part of \mathbf{I} gives the spatial rate of deformation tensor $\mathbf{d} := \text{sym}[\mathbf{I}]$, whereas the skewsymmetric part gives the spin tensor $\mathbf{w} := \text{skw}[\mathbf{I}]$. One finally reaches the following additive split from a multiplicative split¹

$$\mathbf{d} = \mathbf{d}^e + \mathbf{d}^p \quad (\text{A.6})$$

with $\mathbf{d}^e := \text{sym}[\mathbf{I}^e]$ and $\mathbf{d}^p := \text{sym}[\mathbf{I}^p]$. This forms the basis of hypoelastic-plastic formulations which rely on certain objective rates of the selected stress measures.

Appendix B. Hypoelastic-Plasticity

ABAQUS/VUMAT convention is based on a corotational formulation where corotated rate of deformation tensor $\hat{\mathbf{D}}$ is defined as

$$\hat{\mathbf{D}} = \mathbf{R}^t \bullet (\mathbf{d}^e + \mathbf{d}^p) \bullet \mathbf{R} = \hat{\mathbf{D}}^e + \hat{\mathbf{D}}^p. \quad (\text{B.1})$$

with $\hat{\mathbf{D}}^e = \mathbf{R}^t \bullet \mathbf{d}^e \bullet \mathbf{R}$ and $\hat{\mathbf{D}}^p = \mathbf{R}^t \bullet \mathbf{d}^p \bullet \mathbf{R}$. \mathbf{R} denotes the rotation tensor, carried out by the polar decomposition of the deformation gradient, $\mathbf{F} := \mathbf{R} \bullet \mathbf{U}$, with \mathbf{U} representing the symmetric right stretch tensor. Similarly, a pull back operation on \mathbf{T} with the rotation tensor gives the corotated Cauchy stress tensor, $\hat{\mathbf{T}}$,

$$\hat{\mathbf{T}} = \mathbf{R}^t \bullet \mathbf{T} \bullet \mathbf{R}, \quad (\text{B.2})$$

whose material time derivative, $\partial_t \hat{\mathbf{T}}$, can be objectively integrated. Together with the definition of hardening one has

$$\left. \begin{aligned} \partial_t \hat{\mathbf{T}} &= \mathbb{C}^e : \hat{\mathbf{D}}^e \\ q[\alpha] &= K\alpha + (Y^\infty - Y^0)(1 - \exp[-\delta\alpha]) \end{aligned} \right\} \quad (\text{B.3})$$

where \mathbb{C}^e denotes the elastic constitutive tensor with

$$\mathbb{C}^e = \left(\lambda + \frac{2}{3}\mu \right) (\mathbf{1} \otimes \mathbf{1}) + 2\mu \mathbf{I}_{dev}, \quad (\text{B.4})$$

where λ and μ are Lamé's constants and

$$\left. \begin{aligned} \mathbf{I}_{sym} &= \frac{1}{2} (\mathbf{1} \oplus \mathbf{1} + \mathbf{1} \ominus \mathbf{1}), \\ \mathbf{I}_{dev} &= \mathbf{I}_{sym} - \frac{1}{3} (\mathbf{1} \otimes \mathbf{1}), \end{aligned} \right\} \quad (\text{B.5})$$

Appendix C. Numerical Implementation of GTN Model

Letting $\hat{\phi}^p$ represent the yield function defined on corotational stress space with $\hat{\phi}^p = \hat{\phi}^p[\text{dev}[\hat{\mathbf{T}}], \text{tr}[\hat{\mathbf{T}}], f, e^p]$ complete set of equations to be solved can be collected as follows,

$$\left. \begin{aligned} \hat{\mathbf{D}} &= \hat{\mathbf{D}}^e + \hat{\mathbf{D}}^p \neq \mathbf{0}, \\ \partial_t \hat{\mathbf{T}} &= \mathbb{C}^e : \hat{\mathbf{D}}^e, \\ \hat{\mathbf{D}}^p &= \dot{\gamma} \hat{\boldsymbol{\phi}}^p, \\ \partial_t e^p &= \dot{\gamma} \hat{\eta} : \partial_{\hat{\mathbf{T}}} \hat{\phi}^p, \\ \partial_t f &= \dot{\gamma} (A_N \hat{\eta} + \hat{\mathbf{B}}_G) : \partial_{\hat{\mathbf{T}}} \hat{\phi}^p. \end{aligned} \right\} \quad (\text{C.1})$$

with $\hat{\eta} := \hat{\mathbf{T}} / [(1-f)\sigma_y]$. The rotated second order operator, $\hat{\mathbf{B}}_G$, is defined as

$$\hat{\mathbf{B}}_G = \hat{\mathbf{B}}_G(f, \text{dev}[\hat{\mathbf{T}}]) = (1-f)\mathbf{1} + k_{wf} \frac{w(\text{dev}[\hat{\mathbf{T}}])}{\sigma_{eq}} \text{dev}[\hat{\mathbf{T}}]. \quad (\text{C.2})$$

The algorithms utilized in this study fall in the class of cutting plane algorithms. The methods rely on the elastic predictor plastic corrector type operator split. It is assumed that for a typical time step $\Delta t = t_{n+1} - t_n$ the solution at t_n is known as $\{\hat{\mathbf{T}}_n, e_n^p, f_n\}$ and the solution at t_{n+1} is sought for as $\{\hat{\mathbf{T}}_{n+1}, e_{n+1}^p, f_{n+1}\}$. Following abbreviations will be utilized in the formulations for brevity reasons,

$$\hat{\mathbf{r}} := \partial_{\hat{\mathbf{T}}} \hat{\phi}^p, \quad \xi := \partial_{e^p} \hat{\phi}^p, \quad \varsigma := \partial_f \hat{\phi}^p. \quad (\text{C.3})$$

Overall equations will be solved with the operator-split methodology given in Table 4.

Elastic prediction. The elastic prediction for the corotated Cauchy stress $\hat{\mathbf{T}}_{n+1}^{\text{trial}}$ reads

$$\hat{\mathbf{T}}_{n+1}^{\text{trial}} = \hat{\mathbf{T}}_n + \Delta t \partial_t \hat{\mathbf{T}}_{n+1}^{\text{trial}}. \quad (\text{C.4})$$

which relies on integration at the corotational configuration using

¹ Note that for rigid plasticity formulations the elastic part \mathbf{d}^e will be omitted to give $\mathbf{d} = \mathbf{d}^p$.

Table 4

Elastic predictor-plastic corrector type operator split.

Total	Elastic predictor	Plastic corrector
$\left\{ \begin{array}{l} \hat{\mathbf{D}} = \hat{\mathbf{D}}^e + \hat{\mathbf{D}}^p \neq \mathbf{0}, \\ \partial_t \hat{\mathbf{T}} = \mathbb{C}^e : \hat{\mathbf{D}}^e, \\ \hat{\mathbf{D}}^p \neq \mathbf{0}, \\ \partial_t e^p \neq 0, \\ \partial_t f \neq 0. \end{array} \right\}$	$\left\{ \begin{array}{l} \hat{\mathbf{D}} = \hat{\mathbf{D}}^e + \hat{\mathbf{D}}^p \neq \mathbf{0}, \\ \partial_t \hat{\mathbf{T}} = \mathbb{C}^e : \hat{\mathbf{D}}, \\ \hat{\mathbf{D}}^p = \mathbf{0}, \\ \partial_t e^p = 0, \\ \partial_t f = 0. \end{array} \right\}$	$\left\{ \begin{array}{l} \hat{\mathbf{D}} = \hat{\mathbf{D}}^e + \hat{\mathbf{D}}^p = \mathbf{0}, \\ \partial_t \hat{\mathbf{T}} = -\mathbb{C}^e : \hat{\mathbf{D}}^p, \\ \hat{\mathbf{D}}^p = \dot{\gamma} \partial_{\hat{\mathbf{T}}} \hat{\Phi}^p, \\ \partial_t e^p = \dot{\gamma} \hat{\eta} : \partial_{\hat{\mathbf{T}}} \hat{\Phi}^p, \\ \partial_t f = \dot{\gamma} (A_N \hat{\eta} + \hat{\mathbf{B}}_G) : \partial_{\hat{\mathbf{T}}} \hat{\Phi}^p. \end{array} \right\}$

$$\partial_t \hat{\mathbf{T}}_{n+1}^{\text{trial}} = \lambda \text{tr} [\hat{\mathbf{D}}_{n+1}^{\text{e,trial}}] \mathbf{1} + 2\mu \hat{\mathbf{D}}_{n+1}^{\text{e,trial}}, \quad (\text{C.5})$$

with

$$\hat{\mathbf{D}}_{n+1}^{\text{e,trial}} = \hat{\mathbf{D}}_{n+1}, e_{n+1}^{\text{p,trial}} = e_{n+1}^{\text{p}}, f_{n+1}^{\text{trial}} = f_n. \quad (\text{C.6})$$

Within the time step the elastic or plastic character of the status is checked by inserting the trial stress into the yield function,

$$\hat{\Phi}_{n+1}^{\text{p,trial}} = \hat{\Phi}^p [\text{dev} [\hat{\mathbf{T}}_{n+1}^{\text{trial}}], \text{tr} [\hat{\mathbf{T}}_{n+1}^{\text{trial}}], f_{n+1}^{\text{trial}}, e_{n+1}^{\text{p,trial}}], \begin{cases} \leq 0 \Rightarrow \text{elastic}, \\ > 0 \Rightarrow \text{plastic/damage}. \end{cases} \quad (\text{C.7})$$

Once $\hat{\Phi}_{n+1}^{\text{p,trial}} \leq 0$ is satisfied, an elastic state at t_{n+1} is defined and the trial values come out to be admissible which do not require any correction. Otherwise, a plastic correction state, named return mapping, is realized to full/fill the yield condition.

Plastic correction – cutting plane algorithms. For the plastic correction with $\hat{\mathbf{D}} = \mathbf{0}$, one has $\partial_t \hat{\mathbf{T}} = -\dot{\gamma} \mathbb{C}^e : \partial_{\hat{\mathbf{T}}} \hat{\Phi}^p$. This supplies

$$\left. \begin{array}{l} \partial_{\hat{\mathbf{T}}} (\partial_t \hat{\mathbf{T}}) = -\mathbb{C}^e : \partial_{\hat{\mathbf{T}}} \hat{\Phi}^p, \\ \partial_{\hat{\mathbf{T}}} (\partial_t e^p) = \hat{\eta} : \partial_{\hat{\mathbf{T}}} \hat{\Phi}^p, \\ \partial_{\hat{\mathbf{T}}} (\partial_t f) = (A_N \hat{\eta} + \hat{\mathbf{B}}_G) : \partial_{\hat{\mathbf{T}}} \hat{\Phi}^p. \end{array} \right\}. \quad (\text{C.8})$$

The algorithm utilized in the following falls in the class of cutting plane algorithms, Ortiz and Simo (1986), taking advantage of the great generality and implementation convenience proposed. Linearizing the yield function around the current values of variables, calling $\hat{\Phi}_{n+1}^{(i+1)} = \hat{\Phi}^p [\text{dev} [\hat{\mathbf{T}}_{n+1}^{(i+1)}], \text{tr} [\hat{\mathbf{T}}_{n+1}^{(i+1)}], f_{n+1}^{(i+1)}, e_{n+1}^{(i+1)}]$, one has,

$$\begin{aligned} \hat{\Phi}_{n+1}^{(i+1)} &\approx \hat{\Phi}_{n+1}^{(i)} + \hat{\mathbf{r}}_{n+1}^{(i)} \\ &: (\hat{\mathbf{T}}_{n+1}^{(i+1)} - \hat{\mathbf{T}}_{n+1}^{(i)}) + \zeta_{n+1}^{(i)} (e_{n+1}^{(i+1)} - e_{n+1}^{(i)}) \\ &+ \varsigma_{n+1}^{(i)} (f_{n+1}^{(i+1)} - f_{n+1}^{(i)}), \end{aligned} \quad (\text{C.9})$$

The increments read,

$$\left. \begin{array}{l} \hat{\mathbf{T}}_{n+1}^{(i+1)} - \hat{\mathbf{T}}_{n+1}^{(i)} = -\delta\gamma_{n+1}^{(i)} \mathbb{C}^e : \hat{\mathbf{r}}_{n+1}^{(i)}, \\ e_{n+1}^{(i+1)} - e_{n+1}^{(i)} = \delta\gamma_{n+1}^{(i)} \hat{\eta}_{n+1}^{(i)} : \hat{\mathbf{r}}_{n+1}^{(i)}, \\ f_{n+1}^{(i+1)} - f_{n+1}^{(i)} = \delta\gamma_{n+1}^{(i)} (A_{N,n+1}^{(i)} \hat{\eta}_{n+1}^{(i)} + \hat{\mathbf{B}}_{G,n+1}^{(i)}) : \hat{\mathbf{r}}_{n+1}^{(i)}. \end{array} \right\}, \quad (\text{C.10})$$

The incremental plasticity parameter $\delta\gamma_{n+1}^{(i)}$ is computed using

$$\delta\gamma_{n+1}^{(i)} = \frac{\hat{\Phi}_{n+1}^{(i)}}{\hat{\mathbf{r}}_{n+1}^{(i)} : \mathbb{C}^e : \hat{\mathbf{r}}_{n+1}^{(i)} - \zeta_{n+1}^{(i)} \hat{\eta}_{n+1}^{(i)} : \hat{\mathbf{r}}_{n+1}^{(i)} - \varsigma_{n+1}^{(i)} (A_{N,n+1}^{(i)} \hat{\eta}_{n+1}^{(i)} + \hat{\mathbf{B}}_{G,n+1}^{(i)}) : \hat{\mathbf{r}}_{n+1}^{(i)}}. \quad (\text{C.11})$$

This is used in the computation of the new variable updates and the total plasticity parameter $\Delta\gamma$ at the step end through iterations $\Delta\gamma_{n+1}^{(i+1)} = \Delta\gamma_{n+1}^{(i)} + \delta\gamma_{n+1}^{(i)}$ with $\Delta\gamma_{n+1}^{(0)} = 0$. For the update of damage components $\Delta f_{n+1} = \Delta f_{n,n+1} + \Delta f_{g,n+1}$ one has

$$\left. \begin{array}{l} \Delta f_{n,n+1}^{(i)} = \delta\gamma_{n+1}^{(i)} A_{N,n+1}^{(i)} \hat{\eta}_{n+1}^{(i)} : \hat{\mathbf{r}}_{n+1}^{(i)}, \\ \Delta f_{g,n+1}^{(i)} = \delta\gamma_{n+1}^{(i)} \hat{\mathbf{B}}_{G,n+1}^{(i)} : \hat{\mathbf{r}}_{n+1}^{(i)}. \end{array} \right\}. \quad (\text{C.12})$$

Iterations are continued until $\hat{\Phi}_{n+1}^{(i+1)} \leq \text{TOL}$. Finally, the converged corotational stress tensor $\hat{\mathbf{T}}_{n+1}$ should be rotated back to the current configuration using $\mathbf{T}_{n+1} = \mathbf{R}_{n+1} \hat{\mathbf{T}}_{n+1} \mathbf{R}_{n+1}^T$.² As remarked in Ortiz and Simo (1986), above algorithm merely requires essential response function derivations. That is, unlike closest point projection type algorithms, this method does not require a derivation of the Hessian of the yield function. However, as noted in (Simó, 1998 [p. 252]), unlike closest point projection algorithms significant errors may be introduced for large time steps. Thus, the method should better be used only with explicit transient simulations, where the Courant stability condition severely limits the allowable time steps.

References

- Akeret, R., 1978. Failure mechanisms in the bending of Aluminum sheets and limits of Bendability. *Aluminium* 54, 117–123.
- Anderson, T.L., 2004. *Fracture Mechanics: Fundamentals and Applications*. CRC Press.
- Andersson, H., 1977. Analysis of a model for void growth and coalescence ahead of a moving crack tip. *J. Mech. Phys. Solids* 25 (3), 217–233, June.
- Asaro, R.J., 1985. Material modeling and failure modes in metal plasticity. *Mech. Mater.* 4, 343–373.
- ASM Handbooks. 2000. *ASM Handbook*, vol. 8: Mechanical Testing and Evaluation, ASM International.
- Badreddine, H., Saanouni, K., Dogui, A., 2010. On non-associative anisotropic finite plasticity fully coupled with isotropic ductile damage for metal forming. *Int. J. Plast.* 26, 1541–1575.
- Bao, Y., Wierzbicki, T., 2004. On fracture locus in the equivalent strain and stress triaxiality space. *Int. J. Mech. Sci.* 46, 81–98.
- Bao, Y., Wierzbicki, T., 2005. On the cut-off value of negative triaxiality for fracture. *Eng. Fract. Mech.* 72, 1049–1069.
- Barsoum, I., Faleskog, J., 2007. Rupture in combined tension and shear: experiments. *Int. J. Solids Struct.* 44, 1768–1786.
- Beachem, C.D., Yoder, G.R., 1973. Elastic-plastic fracture by homogeneous microvoid coalescence tearing along alternating shear planes. *Metall. Trans.* 4, 1145.
- Becker, R., 1992. An analysis of shear localization during bending of a polycrystalline sheet. *J. Appl. Mech.* 59, 491–496.
- Becker, R., Needleman, A., 1986. Effect of yield surface curvature on necking and failure in porous plastic solids. *J. Appl. Mech.* 53, 491–499.
- Besson, J., 2009. Damage of ductile materials deforming under multiple plastic or viscoplastic mechanisms. *Int. J. Plast.* 25, 2204–2221.
- Bettaieb, M.B., Lemoine, X., Bouaziz, O., Duchêne, L., Habraken, A.M., 2010. A finite element analysis of the bending and the bendability of metallic sheets. *Int. J. Mater. Form.* <http://dx.doi.org/10.1007/s12289-010-0993-8>.
- Bettaieb, M.B., Lemoine, X., Duchêne, L., Habraken, A.M., 2010a. Simulation of the bending process of hardening metallic sheets using damage model. Part I: Theoretical development and numerical implementation. *Mater. Sci. Eng. A* 528, 434–441.
- Bettaieb, M.B., Lemoine, X., Duchêne, L., Habraken, A.M., 2010b. Simulation of the bending process of hardening metallic sheets using damage model. Part II: Numerical investigations. *Mater. Sci. Eng. A* 528, 442–448.
- Bonora, N., Gentile, D., Pironi, A., Newaz, G., 2005. Ductile damage evolution under triaxial state of stress: theory and experiments. *Int. J. Plast.* 21, 981–1007.
- Bonora, N., Ruggiero, A., Esposito, L., Gentile, D., 2006. CDM modeling of ductile failure in ferritic steels: assessment of the geometry transferability of model parameters. *Int. J. Plast.* 22, 2015–2047.
- Broek, D., 1982. *Elementary Engineering Fracture Mechanics*. Springer.
- L.M. Brown J.D. Embury The initiation and growth of voids at second phase particles In Proceedings of the Third International Conference on the Strength of Metals and Alloys, Institute of Metals, London 1973 164
- Brunig, M., 2003. An anisotropic ductile damage model based on irreversible thermodynamics. *Int. J. Plast.* 19, 1679–1713.

² In VUMAT implementation, it should be noted that pre- and post- corotational transformations of tensors are automatically handled by ABAQUS.

- Brunig, M., Ricci, S., 2005. Non-local continuum theory of anisotropically damaged metals. *Int. J. Plast.* 21, 1346–1382.
- Christoffersen, J., Hutchinson, J.W., 1979. A class of phenomenological corner theories of plasticity. *J. Mech. Phys. Solids* 27, 465.
- Dao, M., Lie, M., 2001. A micromechanics study on strain-localization-induced fracture initiation in bending using crystal plasticity models. *Phil. Mag.* 81, 1997–2020.
- Franklin, A.G., 1969. between a quantitative microscope and chemical methods for assessment of non-metallic inclusions. *J. Iron Steel Inst.* 207, 181–186.
- Gurson, A.L., 1977. Continuum theory of ductile rupture by void nucleation and growth – Part I. Yield criteria and rules for porous ductile media. *J. Eng. Mater. Tech.* 99, 2–15.
- Hambli, R., Mkaddem, A., Potiron, A., 2003. Damage prediction in L-bending processes using FEM. *Int. J. Adv. Manuf. Technol.* 22, 12–19.
- Hambli, R., Mkadem, A., Potiron, A., 2004. Finite element damage modeling in bending processes. *J. Mater. Process. Technol.* 147, 302–310.
- Hull, D., 1999. *Fractography: Observing, Measuring and Interpreting Fracture Surface Topography*. Cambridge University Press.
- Jackiewicz, J., 2009. Calibration and evaluation of a combined fracture model of microvoid growth that may compete with shear in polycrystalline microstructure by means of evolutionary algorithms. *Comput. Mater. Sci.* 45, 133–149.
- Kim, J.H., Sung, J.H., Matlock, D.K., Kim, D., Wagoner, R.H., 2010. Finite element and analytical study of plane strain draw-bend failure of advanced high strength steels. *Int. J. Mater. Form* 3, 187–190.
- Kobayashi, S., Oh, S., Altan, T., 1989. *Metal Forming and Finite Element Method*. Oxford University Press.
- Kuroda, M., Tvergaard, V., 2001. Shear Band development predicted by an non-normality theory of plasticity and comparison to crystal plasticity predictions. *Int. J. Solids Struct.* 38, 8945–8960.
- Kuroda, M., Tvergaard, V., 2004. Shear band development in anisotropic bent specimens. *Eur. J. Mech. A/Solids* 23, 811–821.
- Kuroda, M., Tvergaard, V., 2007. Effects of texture on shear band formation in plane strain tension/compression and bending. *Int. J. Plast.* 23, 244–272.
- Lemaitre, J., 1996. *A Course on Damage Mechanics*. Springer-Verlag, Berlin.
- Lemaitre, J., Desmorat, R., 2005. *Engineering Damage Mechanics*. Springer-Verlag, Berlin Heidelberg.
- Le Maoût, N., Thuillier, S., Manach, P.Y., 2009. Aluminum alloy damage evolution for different strain paths – Application to hemming process. *Eng. Fract. Mech.* 76, 1202–1214.
- Lemonds, J., Needleman, A., 1986. Finite element analysis of shear localization in rate and temperature dependent solids. *Mech. Mater.* 5, 339–361.
- Lievers, W.B., Pilkey, A.K., Lloyd, D.J., 2003a. The influence of iron content on the bendability of AA6111 sheet. *Mater. Sci. Eng.* 361, 312–320.
- Lievers, W.B., Pilkey, A.K., Worswick, M.J., 2003b. The co-operative role of voids and shear bands in strain localization during bending. *Mech. Mater.* 35, 661–674.
- Gharbi, Malekipour, M., Labergere, C., Badreddine, H., Soyarslan, C., Weinrich, A., Hermes, M., Chatti, S., Sulaiman, H., Saanouni, K., Tekkaya, A.E., 2011. Advanced experimental-numerical investigations of cold bending of high strength steels, steel research international Special Edition: 10th International Conference on Technology of Plasticity, ICTP2011, pp. 877–883.
- Mear, M.E., Hutchinson, J.W., 1985. Influence of yield surface curvature on flow localization in dilatant plasticity. *Mech. Mater.* 4, 395–407.
- Menzel, A., Ekh, M., Runesson, K., Steinmann, P., 2005. A framework for multiplicative elastoplasticity with kinematic hardening coupled to anisotropic damage. *Int. J. Plast.* 21, 397–434.
- Meyers, M.A., Chawla, K.K., 2009. *Mechanical Behavior of Materials second ed.* Cambridge University Press.
- Nahshon, K., Hutchinson, J.W., 2008. Modification of the Gurson model to shear failure. *Eur. J. Mech. A/Solids* 27, 1–17.
- Nahshon, K., Xue, Z., 2009. A modified Gurson model and its applications to Punch-out experiments. *Eng. Fract. Mech.* 76, 997–1009.
- Needleman, A., Rice, J.R., 1978. Limits to ductility set by plastic flow localization. In: Koistinen (Ed.), *Mechanics of Sheet Metal Forming*, Plenum Press, New York, p. 237.
- Nielsen, K.L., Tvergaard, V., 2009. Effect of a shear modified Gurson model on damage development in a FSW tensile specimen. *Int. J. Solids Struct.* 46, 587–601.
- Nielsen, K.L., Tvergaard, V., 2010. Ductile shear failure or plug failure of spot welds modelled by modified Gurson model. *Eng. Fract. Mech.* 77, 1031–1047.
- Ortiz, M., Simo, J.C., 1986. An analysis of a new class of integration algorithms for elastoplastic constitutive relations. *Int. J. Numer. Methods Eng.* E 23, 353–366.
- Oudin, J., Bennani, B., Picard, P., 1995. models for microvoid nucleation, growth and coalescence in elastoplasticity, finite element reference modelling. In: Ghosh, S.K., Predeleanu, M., Eds., *Material Processing Defects*, 107–122. Elsevier Science B.V.
- Pirondi, A., Bonora, N., Steglich, D., Brocks, W., Hellmann, D., 2006. Simulation of failure under cyclic plastic loading by damage models. *Int. J. Plast.* 22, 685–712.
- Poruks, P., Yakubtsov, I., Boyd, J.D., 2006. Martensite-ferrite interface strength in a low-carbon bainitic steel. *Scr. Mater.* 54, 41–45.
- Saje, M., Pan, J., Needleman, A., 1980. Void nucleation effects on shear localization in porous plastic solids. Report NSF-ENG76-16421/7 Brown University.
- Sarkar, J., Kutty, T.R.G., Conlon, K.T., Wilkinson, D.S., Embury, J.D., Lloyd, D.J., 2001. Tensile and bending properties of AA5754 aluminium alloys. *Mater. Sci. Eng. A* A316, 52–59.
- Simó, J.C., 1998. Numerical analysis and simulation of plasticity. *Handbook Numer. Anal.* 6, 183–499.
- Soyarslan, C., Tekkaya, A.E., 2010. A damage coupled orthotropic finite plasticity model for sheet metal forming: CDM approach. *Comput. Mater. Sci.* 48, 150–165.
- Soyarslan, C., Tekkaya, A.E., Akyuz, U., 2008. Application of continuum damage mechanics in discontinuous crack formation: forward extrusion chevron predictions. *Z. Angew. Math. Mech.* (88/6), 436–453.
- Tasan, C., 2010. *Micro-Mechanical Characterization of Ductile Damage in Sheet Metal*. Ph.D. Thesis, Eindhoven University of Technology (TU/e).
- Triantafyllidis, N., Needleman, A., Tvergaard, V., 1982. On the development of shear bands in pure bending. *Int. J. Solids Struct.* 18, 121–138.
- Tvergaard, V., 1981. Influence of voids on shear band instabilities under plane strain conditions. *Int. J. Fract.* 17, 389–407.
- Tvergaard, V., 1982a. On localization in ductile materials containing spherical voids. *Int. J. Fract.* 18, 237–252.
- Tvergaard, V., 1982b. Influence of void nucleation on ductile shear fracture at a free surface. *J. Mech. Phys. Solids* 30, 399–425.
- Tvergaard, V., 1987. Ductile shear fracture at the surface of a bent specimen. *Mech. Mater.* 6, 53–69.
- Tvergaard, V., Needleman, A., 1984. Analysis of cup-cone fracture in a round tensile bar. *Acta Mater.* 32, 157–169.
- Wisselink, H.H., Huetink, J., 2007. Application of nonlocal damage models to sheet forming applications. In: COMPLAS 2007, IX International Conference on Computational Plasticity, Barcelona.
- Wisselink, H.H., Huetink, J., 2008. Prediction of the bendability of sheet metals using nonlocal damage models. *Mater. Innovat. Inst.* 1, 217–224.
- Wisselink, H.H., Huetink, J., 2009. Modelling of ductile failure in metal forming, Europe LS-DYNA Conference.
- Xue, L., Wierzbicki, T., 2008. Ductile fracture initiation and propagation modeling using damage plasticity theory. *Eng. Fract. Mech.* 75, 3276–3293.
- Yamamoto, H., 1978. Conditions for shear localization in the ductile fracture of void-containing materials. *Int. J. Fract.* 14, 347.